# Radiation pattern measurement method for on-wafer mm-wave antenna

**Gaurav Khairkar**

**School of Electrical Engineering**

Thesis submitted for examination for the degree of Master of Science in Technology.

Espoo 23.05.2016

**Thesis supervisor:**

Prof. Antti Räisänen

**Thesis advisor:**

D.Sc. (Tech.) Juha Ala-Laurinaho

Aalto University
School of Electrical
Engineering

AALTO UNIVERSITY
SCHOOL OF ELECTRICAL ENGINEERING

ABSTRACT OF THE
MASTER'S THESIS

Author: Gaurav Khairkar

Title: Radiation pattern measurement method for on-wafer mm-wave antenna

Date: 23.05.2016 Language: English Number of pages: 8+43

Department of Radio Science and Engineering

Professorship: Radio Science and Engineering

Supervisor: Prof. Antti Räisänen

Advisor: D.Sc. (Tech.) Juha Ala-Laurinaho

With the advent of new technology, the manufacture of high-frequency antennas and RFIC's has become feasible. This has led to smaller and smaller antennas in the mm-wave frequency range. The traditional techniques used for antenna characterization may be problematic for small probe-fed antennas. To counter these problems, radiation pattern retrieval (RPR) method has been developed. RPR is dependent on the reflection coefficients obtained from placing a reflective load in the near-field of the antenna. RPR method is implemented using inversion algorithm. Multiple reflections can cause errors in RPR as it considers only the first reflection from reflective load. To address this issue, time gating method is investigated.

The purpose of this thesis is to study radiation pattern retrieval for on-wafer antennas, especially to improve RPR method using multiple reflection mitigation, implemented using time gating. To experimentally test this hypothesis, a 4x4 patch array is designed for 77 GHz. A reflective copper strip is placed at 90 mm or 120 mm distance from the antenna. The width of the strip is 30 mm and 60 mm and it is moved in 1.95 mm steps from -39 mm to +39 mm offset positions. A VNA measures the $S_{11}$ at each position which is Fourier transformed into its time domain signal, time gated and then transformed back to the frequency domain. The new $S_{11}$ is used to observe the effects on the radiation pattern. The copper strip configurations with different widths and distance help test the repeatibility of the experiment.

Time gating is estimated to remove unwanted reflections, however, inconclusive results suggest the need for exhaustive study of the inversion algorithm and RPR model. More qualitative study of multiple reflection reduction techniques would give a deeper insight in their effect on radiation pattern retrieval.

Keywords: mm-wave, antenna, antenna measurements, multiple reflection, radiation pattern, time gating, inversion algorithm, on-wafer

# Preface

This Master's thesis was carried out in the Millimetre wave and THz techniques research group in the Department of Radio Science and Engineering (RAD) of the Aalto University School of Electrical Engineering between May 2015 and May 2016. The measurements for this research were conducted at RAD in MilliLab, which is a joint institute between VTT Technical Research Centre of Finland and Aalto University, and an external laboratory of European Space Agency (ESA).

I would like to thank Professor Antti Räisänen for providing me with the opportunity to work here, to guide me in my times of frustration and for supervising my thesis. I would also like to thank my instructor Juha Ala-Laurinaho, D.Sc (Tech.) for his guidance throughout the process of this thesis. I thank him for his patience, when I panicked and made last minute result submissions. I am very grateful to Juha for pushing me to work hard and publish a paper as well as motivating me to finish my thesis. It has been a wonderful learning experience to work here in RAD. I express my gratitude to all my colleagues who provided me with valuable feedback and guidance.

Lastly, I would like to thank my friends and my parents, for their support and encouragement, and who made this last one year, a memorable journey. This thesis is for all of you!

Otaniemi, Espoo, 23.05.2016

Gaurav Khairkar

# Contents

# Symbols and abbreviations

## Symbols

| | |
|---|---|
| $A$ | Length of aperture of horn antenna |
| $B$ | Width of aperture of horn antenna |
| $D$ | Largest dimension of antenna aperture |
| $E_{AUT}(x, y, z)$ | Electrical aperture field distribution |
| $E_\Gamma$ | Electrical field distribution after reflection at the reflecting strip |
| $f_r$ | Resonant frequency |
| $h$ | Height of the substrate |
| $\bar{k}$ | Wave vector |
| $k_x$ | $x$-component of wave vector |
| $k_y$ | $y$-component of wave vector |
| $k_z$ | $z$-component of wave vector |
| $L$ | Length of reflective strip |
| $L_{horn}$ | Distance between the horn antenna aperture and waveguide |
| $L_p$ | Length of patch |
| $L_{WG}$ | Length of waveguide |
| $S_{11}$ | Reflection coefficient at input port of AUT |
| $S_{11,aperture}$ | Reflection coefficient at the aperture of the antenna |
| $S_{11,static}$ | Reflection coefficient measured with no reflective strip |
| $S_{11,n}$ | Reflection coefficient measured at position n |
| $P_{AUT}(k_x, k_y, z)$ | Plane Wave Spectrum form of the electrical aperture field distribution |
| $P_\Gamma(k_x, k_y, z)$ | Plane Wave Spectrum form after reflection |
| $R$ | Far-field distance |
| $S$ | Aperture surface |
| $t_{fsr}$ | Reflected time domain signal with no reflective strip |
| $t_i$ | Reflected time domain signal with reflective strip at position i |
| $t_{i,final}$ | Final reflected time domain signal |
| $W$ | Width of the strip |
| $W_p$ | Width of the patch |
| $X_{move}$ | Movement range of the reflective strip |
| $Z$ | Impedance |
| $z_0$ | Distance between antenna aperture and reflecting load |
| $\alpha$ | Attenuation constant |
| $\Gamma(x, y)$ | Spatial reflection coefficient |
| $\Delta$ | Cost-Function |
| $\Delta L_p$ | Difference in the length of the patch |
| $\epsilon_0$ | Permittivity in vacuum |
| $\epsilon_r$ | Relative permittivity of the substrate |
| $\epsilon_{reff}$ | Effective permittivity for the electromagnetic wave |
| $\theta$ | Phase delay |
| $\theta_{valid}$ | Valid angular region |
| $\lambda$ | Wavelength |
| $\mu_0$ | Permeability in vacuum |

## Operators

| | |
|---|---|
| $\lvert\bar{k}\rvert$ | Magnitude of vector |
| $\int\int_S$ | Integrate over the surface area |
| $FT$ | Fourier transform |
| $FT^{-1}$ | Inverse Fourier transform |
| $*$ | Convolution |
| $\sum_n$ | Summation |

## Abbreviations

| | |
|---|---|
| AUT | Antenna Under Test |
| CATR | Compact Antenna Test Range |
| CST | Circuit Simulation Technology |
| CF | Cost-Function |
| CF1 | Cost-Function 1 |
| CF2 | Cost-Function 2 |
| CRP | Center Reflection Position |
| E-Band | 71-76 GHz and 81-86 GHz bands |
| FT | Fourier Transform |
| FSR | Free Space Response |
| GSG | Ground-Signal-Ground |
| IFT | Inverse Fourier Transform |
| IoT | Internet of Things |
| PEC | Perfect Electric Conductor |
| PWS | Plane Wave Spectrum |
| RFIC | Radio Frequency Integrated Chip |
| RPR | Radiation Pattern Retrieval |
| VNA | Vector Network Analyzer |

# 1 Introduction

Nowadays, smartphones, wearables and other IoT devices have become ubiquitous. Each of them has a wired/wireless connection to send and receive data. The number of consumer devices is continuously increasing at a steady rate. We are headed to a time where all devices will be interconnected. This interconnected system, to function in a smooth manner, requires massive data transfer between different IoT devices, smartphones and the world wide web. These systems will be connected wirelessly. Considering the massive data transfer -with the demand for high quality, real time information on the rise- wireless connectivity required to fulfill this demand, the hiking ubiquity of connected devices, insists on a large spectrum requirement. Jumping back to the present, we have exhausted usable spectrum upto 30 GHz using the current data communication technology [1].

The obvious answer to solving the bulging high data rate demand and increasing data transfer devices is to use the spectrum above 30 GHz. This is where mm-wave band enters the picture. The mm-wave band stretches from 30 GHz-300 GHz. All the current data communication technology can be incorporated in the lower 30 GHz of the mm-wave band. Theoretically, a large bulk of underutilized spectrum is available at our disposal. The current cellular communication system utilizes spectrum upto 5 GHz. The E-band, which goes from 71-76 GHz and 81-86 GHz covers a bandwidth of 10 GHz and easily covers the capacity of the 5 GHz band we use currently [2]. Waves at mm-wave frequencies have a smaller propagation range, catering to a smaller crowd. This leads to less interference and higher data rate, because of the availability of more bandwidth. The above argument proposes technology to be developed for mm-wave spectrum. Hence, the development of mm-wave antennas and RFIC's for the mm-wave band, has been advanced in the last few years. The size of mm-wave antennas has shrunk with the advent of new technologies.

Radiation pattern is an important property of any antenna. The radiation pattern is used to characterize the antenna. For example, the radiation pattern of a horn antenna often has a symmetric main lobe. As the radiation pattern of the horn is known, the antenna can be characterized accordingly. Knowledge of the radiation pattern of the antenna can be used for different applications. Traditionally, radiation pattern has been measured in far-field, near-field or Compact Antenna Test Range (CATR). In the far-field technique, a reference antenna is placed in the far-field of the Antenna Under Test (AUT). The AUT is rotated and radiation pattern at rotation steps is measured by the reference antenna. In the near-field technique [3],[4], the near-field of the antenna is probed and the near-field distribution is used to calculate the radiation pattern of the antenna. For electrically large antennas, CATR or near-field range is used, as the far-field distance of these antennas is large. This follows from the formula, $R = 2D^2/\lambda$, where, $R$ is the far-field distance, $D$ is the largest dimension of the antenna aperture and $\lambda$ is the wavelength. In this case, a collimating element such as a reflector or lens is used to generate the planar wavefront, representing far-field conditions.

Small mm-wave antennas are many times accessible only with probe stations. When measurements are done using probe stations, the antenna is fed with an on-

wafer probe and fixed in one position. There are problems to measure the radiation pattern of small mm-wave probe fed antennas using traditional techniques mentioned above. First, the AUT cannot be rotated to perform the far-field method to attain radiation pattern. Even if the measurement is to be done by moving the reference antenna, the probe station environment makes it inconvenient to do so. Second, at mm-wave frequencies, bending of cables can cause phase errors in the near-field distribution. In the near-field measurement method, this discrepancy can lead to erroneous radiation pattern calculation. Third, movement of near-field probe is impeded by probe station apparatus, microscopes attached etc.

To address problems mentioned above, a Radiation Pattern Retrieval (RPR) method [5] is developed. A reflective load with known properties is translated in the near-field of the AUT. This way no bending of cables or moving of AUT is involved. Reflection coefficients ($S_{11}$) measured at each position of the load are fed into the inversion algorithm. This algorithm is used in the RPR method to obtain the radiation pattern. The inversion algorithm used in RPR considers only single reflection. Multiple reflections can change the $S_{11}$, causing the RPR method to calculate an erroneous radiation pattern.

This thesis presents an investigation of the robustness of the inversion algorithm. In addition, the thesis focuses on tackling the problem of multiple reflection by the application of time gating. The theoretical verification of time gating and inversion algorithm are first done with a horn antenna operating at 30 GHz. A horn antenna is used because it has a well known radiation pattern and is easier to investigate based on the information available. Later, an on-wafer antenna, designed to operate at 77 GHz, is simulated, fabricated and used for experimental verification.

The thesis is structured as follows: Chapter 2 provides detailed information on the RPR method and the underlying theory. Chapter 3 discusses the method to mitigate multiple reflections and how they are implemented. Chapter 4 details the process to design the 77 GHz on-wafer antenna. Variety of results are discussed and analyzed in chapter 5. Chapter 6 presents the summary of the thesis.

# 2 Radiation pattern retrieval

## 2.1 Antenna measurement methods

Typically, radiation pattern of antenna is measured using one of the three methods, far-field, near-field and CATR.

**Far-Field Method:**

Figure 1 displays the experimental setup for the far-field method to measure radiation pattern of an antenna.

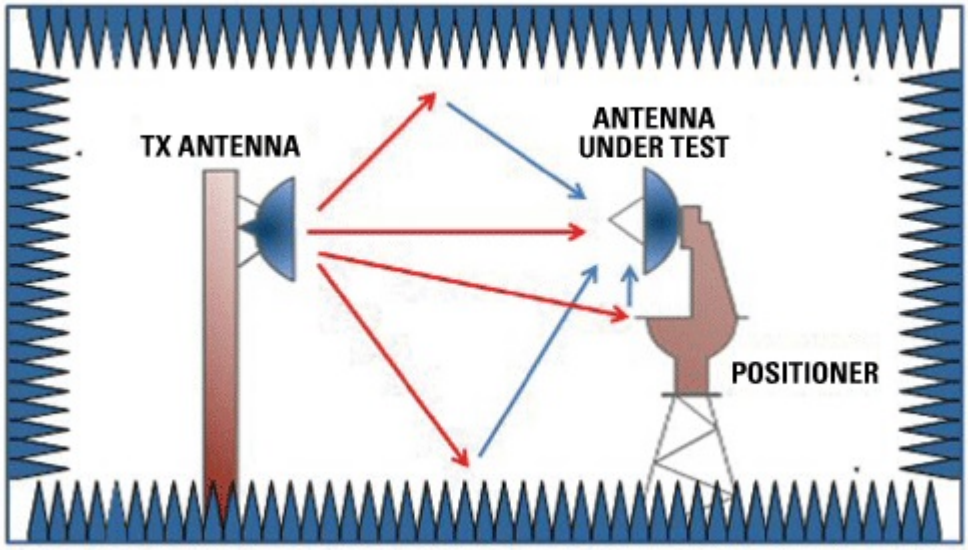


Figure 1: Farfield measurement setup [6].

The far-field method is the most commonly used method to determine far-field characteristics of AUT. The reference antenna and AUT are placed in an anechoic chamber. An anechoic chamber is a room lined with absorbent material, the purpose of which is to avoid stray reflections, which could interfere with transmission and reflection properties of the antennas. The antennas are placed in the far-field range of each other. The reference antenna transmits power. AUT at the receiver end is rotated and the received power at each position is recorded. The AUT can also transmit power while the reference antenna receives power. These measurements form a polar plot of radiation pattern in the azimuthal/elevation plane. The AUT is then rotated in the elevation/azimuthal plane. The experiment is often repeated many times to test the repeatability of the measurements.

**Near-field method:**

The near-field method is a quite straightforward method, however, consisting of a lot more post-processing as compared to the previous method. A near-field probe scanner is used to perform this method. The near-field probe, as it states, is moved in

the near-field of the AUT. The probe, can move in the planar, cylindrical, or spherical plane in the proximity of the antenna [4]. The purpose of the near-field scanner is to measure enough points to be able to map the near field distribution accurately. The measured near-field distribution is then post-processed to get the far-field. This method proves to be useful to measure large antennas. Near-field method is subject to errors in measurement for high frequency operation. The bending of cables can cause phase changes. Movement in the spherical and cylindrical plane, usually requires a complicated experimental setup.

**Compact Antenna Test Range(CATR) method:**

Figure 2 displays the experimental setup for the hologram based CATR method to measure radiation pattern.

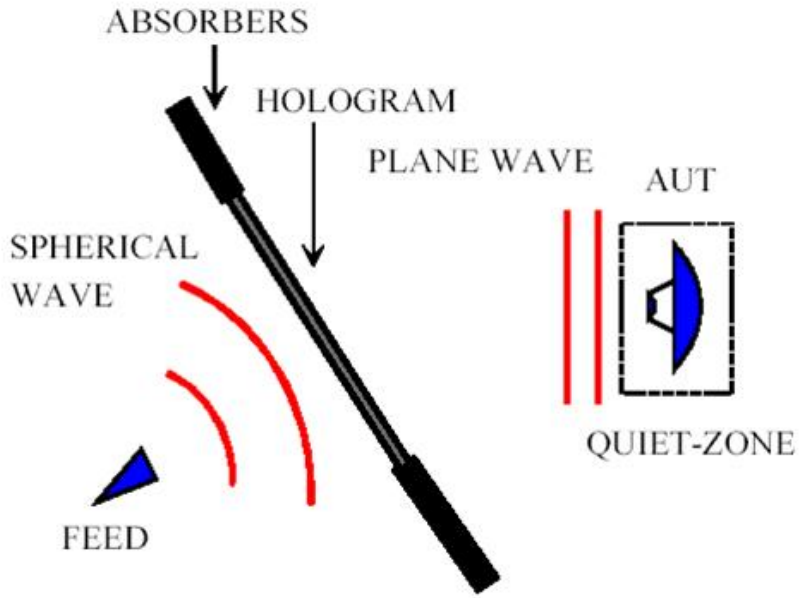


Figure 2: A hologram based CATR measurement setup [7].

The CATR method emulates the environment described in the far-field method. The antenna is considered to be in the far-field, if the wave propagating towards it forms a planar wavefront. This can be achieved by using a hologram, lens or reflector as a collimating element. The far-field method described above is performed with this additional setup to attain the radiation pattern in a smaller anechoic chamber. This eliminates the limitation of measuring large antennas, at the expense of inducing additional complexity in handling the experimental setup. At higher frequencies, a hologram is easier to manufacture than a reflector or lens. Consequently, a hologram CATR is very attractive for mm/submm-wave bands. However, being a frequency sensitive element, the operation bandwidth is usually limited to 5-10% [8].

## 2.2 Problems to measure radiation pattern of on-wafer antennas

For a large antenna, the anechoic chamber required to place the AUT in the far-field, can be very big, according to the far-field range requirement of, $R = 2D^2/\lambda$, where $R$ is the distance from the antenna. The far-field method is thus, not convenient in all the cases. In [10], [11], [12], [13], complicated mechanical arms are used for the probe movements around AUT. At mm/submm-wave frequencies, on-wafer measurements encounter further challenges. Flexing of cables leads to phase changes in the field distribution. This is because the electrical length of the connecting cable is quite large compared to the wavelength [5].

The focus of this thesis is to measure mm-wave on-wafer antennas. On-wafer antennas are fed by coplanar probes [14]. Coplanar probes feed the antenna in the Ground-Signal-Ground (GSG) configuration, where the tip of the probes touch the metallic pads. The tip of the probe is prone to breakage, if excess force is exerted on it.

Figure 3 shows a coplanar GSG probe used for on-wafer antenna measurement.


Figure 3: Coplanar probe [9].

In the above methods, antennas are connected to measurement equipment with cables that, when displaced, easily change their electrical length. At high frequencies, even a small change in the cable geometry can lead to a big phase change to the transmitted/received signal. The Radiation Pattern Retrieval (RPR) method is developed to measure antennas without flexing cables and moving antennas.

## 2.3 Literature survey of antenna measurement methods using reflection coefficients

The RPR method discussed in this thesis is similar in some respects to work done before. Antenna measurements for large reflector antenna require big antenna measurement range [15]. Thus, CATR were used to measure these antennas. Compact Antenna Test Ranges are expensive. A relatively inexpensive way to measure antennas, in a compact configuration was developed [15],[16]. The method described, used

only an additional plane reflecting surface, to provide complete reflection, neglecting propagation loss.

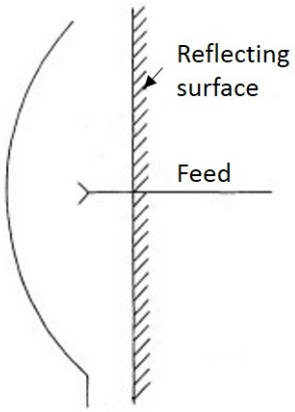


Figure 4: Compact gain measurement setup.

The return loss measured at the antenna feed is the total loss figure. This comprises of twice the losses of one way transmission. The loss figure is directly proportional to the gain of the antenna. Thus, this method can be used to find the relative gains of a group of antennas with similar geometry.

The near-field wire scattering method in [17], is only capable of solving radiation pattern in one cut. Moreover, the near-field distributions of the antenna have to be separable to be able to implement this technique. This technique requires the near-field distribution to be separable. Separable near-field distribution, restricts the applicability of this method. Furthermore, the far-field solution is only in the azimuthal or elevation plane.

## 2.4 Theory of radiation pattern retrieval method

The Radiation Pattern Retrieval method allows compact measurements of antennas, without complicated experimental setup. In this thesis, the RPR method is used to measure on-wafer mm-wave antennas, which are measured using a probe. This method makes it easier to measure them, without implementing rotating arms and complicated experimental setup. The RPR method has the advantage of performing even with non-separable near-field distribution. It circumvents the problem of flexing cables. This keeps the setup stable and free of unwanted phase changes. The theoretical basis for the RPR method is presented here [5].

The antenna has an electrical aperture field distribution of $E_{AUT}(x, y, z)$. The ratio between the electric and magnetic field is the free space wave impedance. The reflection coefficient of the reflecting plane is $\Gamma(x, y)$. A reflective plane with known characteristics is placed in the near-field of the antenna. To test the viability of the RPR method, it is implemented on a horn antenna at 30 GHz.

The electric field distribution can be written in the Plane Wave Spectrum (PWS) form. This is done by applying Fourier transform to the field distribution at the

aperture of the antenna,

$$P_{AUT}(k_x, k_y, z = 0) = \frac{1}{2\pi} \int \int_S (E_{AUT}(x, y, z = 0)) e^{j(k_x x + k_y y)} dx dy \tag{1}$$

where $S$ is the aperture surface, $k_x$ and $k_y$ are $x$ and $y$ components of the wave vector ($|\bar{k}| = k = 2\pi/\lambda$). The assignment $z = 0$ signifies the location of the calculation, which in this case is at the aperture surface.

The electric field distribution is converted to PWS form, so that the electric field distribution at the reflective plane surface can be calculated. This is done by propagating the field distribution by $z_0$. It is propagated using,

$$P_{AUT}(k_x, k_y, z = z_0) = P_{AUT}(k_x, k_y, z = 0) e^{-jk_z z_0} \tag{2}$$

where $k^2 = k_x^2 + k_y^2 + k_z^2$.
The field at the reflective plane surface is,

$$E_{AUT}(x, y, z = z_0) = \frac{1}{2\pi} \int_{-k}^{k} \int_{-k}^{k} (P_{AUT}(k_x, k_y, z = z_0)) e^{-j(k_x x + k_y y)} dk_x dk_y \tag{3}$$

The reflected field distribution at the antenna aperture is obtained by multiplying $E_{AUT}(x, y, z = z_0)$ and reflection coefficient of the surface and propagating it back, resulting in:

$$E_\Gamma(x, y, z = 0) = FT\{FT^{-1}\{E_{AUT}(x, y, z = z_0)\Gamma(x, y)\} e^{-jk_z z_0}\} \tag{4}$$

The reflection coefficient at the antenna aperture is obtained using the following relation,

$$S_{11,aperture} = \frac{\int \int_S E_\Gamma(x, y, z = 0) E_{AUT}(x, y, z = 0) d_x d_y}{\int \int_S E_{AUT}(x, y, z = 0) E^*_{AUT}(x, y, z = 0) d_x d_y} \tag{5}$$

where * denotes the complex conjugate, $E_\Gamma(x, y, z = 0)$ is the reflected field distribution at the antenna aperture and $S_{11,aperture}$ is the reflection coefficient at the antenna aperture.
The reflection coefficient at the antenna feed is,

$$S_{11} = e^{2(j\theta - \alpha)} S_{11,aperture} + S_{11,static} \tag{6}$$

where $\theta$ is phase delay, $\alpha$ is attenuation constant between the antenna feed and aperture plane and $S_{11,static}$ is the reflection coefficient measured at the feed when no reflecting plane is present. The antenna aperture field can be obtained by iteratively solving Equations (1)-(6). The least-squares fitting method is used to minimize $\Delta$. $\Delta$ is also called the cost-function:

$$CF1 = \Delta = min_{E_{AUT}, \alpha} \sum_n |S_{11,aperture}(E_{AUT}, \Gamma_n(x, y)) e^{-2\alpha} + S_{11,static} - S_{11,n}|^2 \tag{7}$$

$$CF2 = min_{E_{AUT},\alpha} \sum_{n} |S_{11,aperture}(E_{AUT}, \Gamma_n(x,y))e^{-2\alpha} + S_{11,static} - S_{11,n}|^2 \int |\frac{dE_{AUT}}{dx}|dx \tag{8}$$

The cost-function used in Equation (7), is the best estimator when the reflection coefficient is corrupted by additive white Gaussian noise [5]. This cost-function is cost-function 1 (CF1) The aperture field obtained using CF1, may have large spatial disturbance. However, the aperture field of an antenna is usually smooth. To favor the smooth varying aperture field the cost-function was modified [19]. This cost-function is cost-function 2 (CF2). Equation (8) shows the modified cost-function.

A simple flowchart is presented in Figure 5, to give the reader a better understanding of the RPR method. This method involves a lot of calculations for each iteration step [18]. The process involves Fourier transformation at the aperture of the antenna. The inverse process is done again in the final step as seen in Figure 5.

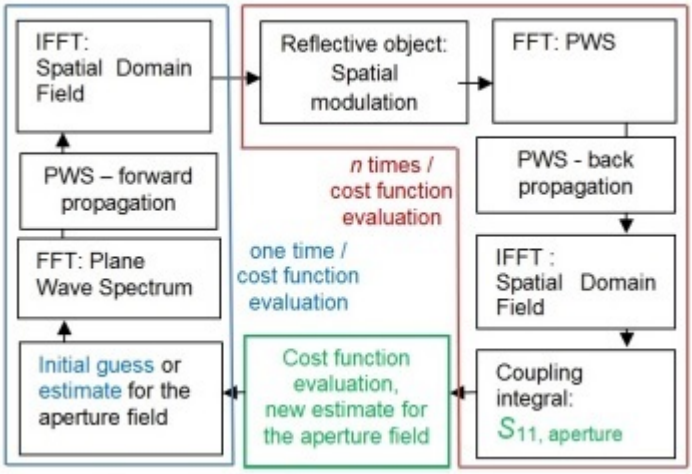


Figure 5: Flowchart of RPR method [18].

A modification to this process is proposed to hasten the output time [18]. The coupling integral between the aperture field and corresponding reflected field is replaced by the convolution between the PWS functions of the corresponding fields [18]:

$$S_{11,aperture} = \frac{P_\Gamma(k_x, k_y, z=0) * P_{AUT}(k_x, k_y, z=0)}{P_{AUT}(k_x, k_y, z=0) * P_{AUT}(k_x, k_y, z=0)} \tag{9}$$

The modified flowchart is displayed in Figure 6.

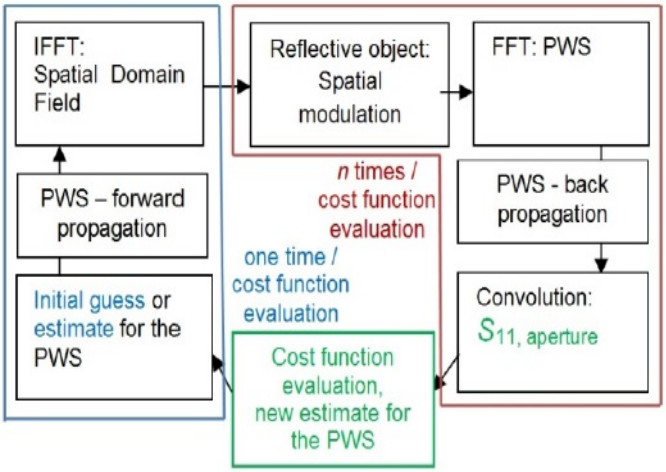


Figure 6: Flowchart of RPR method modified for optimization [18].

## 2.5 Implementation of radiation pattern retrieval method for a horn antenna

Figure 7 displays the measurement setup schematic for the horn antenna. $A$ and $B$ are the dimensions of the antenna aperture. A reflective strip with a 25 mm width ($W$) and 125 mm length ($L$)is placed in front of the antenna at a distance of $z = z_0 = 60$ mm. As the theory does not consider evanescent modes, present in the reactive near-field of the antenna, the reflective strip needs to be placed outside it. For electrically large antennas, the reactive near-field region ends at $z \geq 0.62\sqrt{D^3}/\lambda$, where $D$ is the maximum dimension of the antenna aperture. [5]

One more factor determining the movement limits of the reflective strip along the x-axis, is the valid angular region. The RPR method is ineffective in estimating the radiation pattern outside this region. The valid angular region can be approximated from the geometry of the measurement setup:

$$\theta_{valid} = \tan^{-1}\left(\frac{X_{move} - D}{2z_0}\right) \tag{10}$$

where $\theta_{valid}$ is the valid angle and $X_{move}$ is the movement range of the reflective strip as displayed in Figure 7.

The reflective strip is moved with a 5 mm offset and reflection coefficients are measured at each instance. $X_{move}$ goes from -40 mm to +40 mm in 5 mm steps. These are then post-processed in MATLAB to obtain the far-field pattern. This experimental setup is also simulated using CST and the $S_{11}$ in the simulations are also compared to get a better understanding of the viability of this method. After evaluating the results, further experiments were performed with this method to observe their effect to the output obtained from the horn antenna experiment.

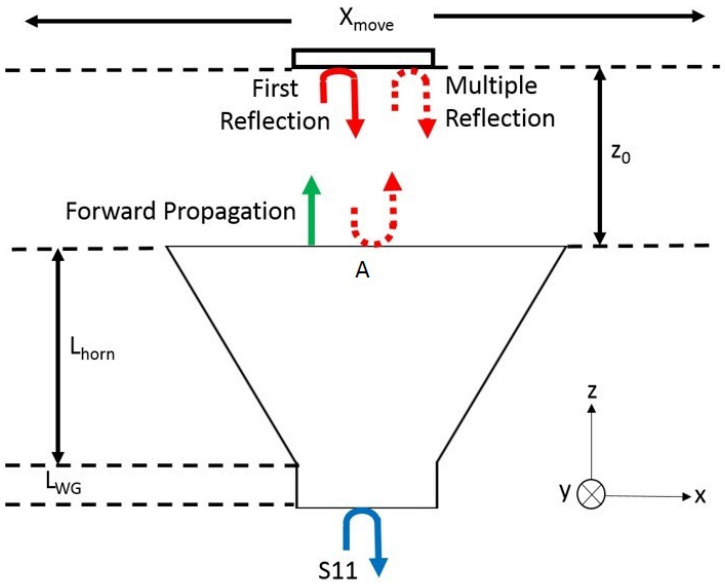


Figure 7: Measurement setup schematic.

Table 1 mentions the dimensions of the experimental setup. A and B are the length and width of the antenna aperture.

Table 1: Dimensions for setup in Figure 7 [5].

| **Parameter** | **Value(mm)** | **Parameter** | **Value(mm)** |
|---|---|---|---|
| W | 25 | $L_{horn}$ | 55.35 |
| L | 125 | $L_{WG}$ | 15 |
| A | 37.85 | $z_0$ | 60 |
| B | 28.45 | | |

The reflection coefficient results and the radiation pattern from the simulation of the setup are used in post-processing. Figure 8 displays the reflection coefficients plot. The reflection coefficients at different positions are plotted. The blue curve represents simulated reflection coefficients ($S_{11,n}$) at 30 GHz. The red curve displays the fitted reflection coefficients ($S_{11}$) after implementing RPR. This data is extracted

for 30 GHz. Radiation pattern obtained, using the RPR method is compared with the radiation pattern of the horn antenna obtained from CST simulation in Figure 9. The red curve displays the radiation pattern obtained using the RPR method and the blue curve displays the radiation pattern from CST simulation. The radiation pattern displayed hereafter is in the $\phi = 90°$ plane. Observing the plots, the dissimilarity between the reflection coefficients seems to be small. The radiation patterns shows divergent behavior outside the $-20°$ to $+20°$. The next two figures explore, how the variation in the cost-function affects the radiation pattern.

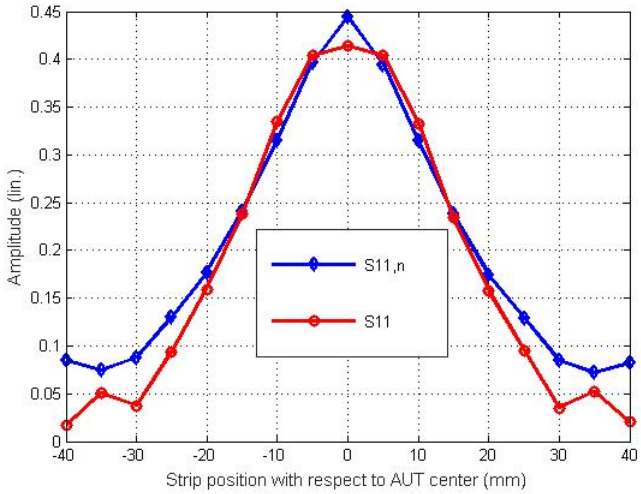


Figure 8: Reflection coefficients from CST ($S_{11,n}$) and estimated reflection coefficients using RPR method ($S_{11}$) at 30 GHz.

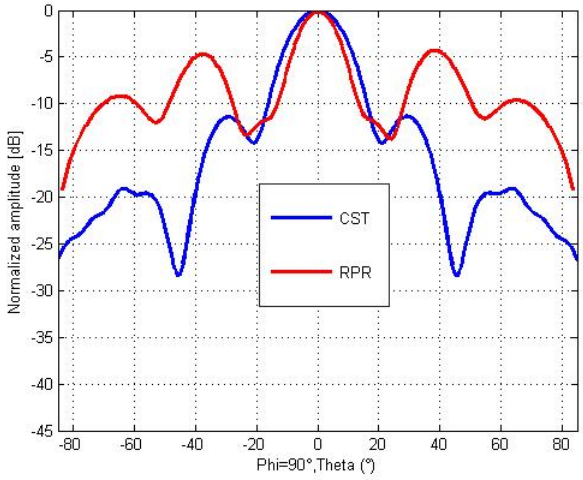


Figure 9: Radiation pattern from CST and radiation pattern retrieved with RPR using $S_{11}$.

Figure 10 and Figure 11 show reflection coefficient and radiation pattern at 30 GHz for CF1 and CF2. The plots for CF1 and CF2 are compared with the simulated in CST results for the horn antenna. As observed in Figure 11, the CF1 plot estimates the radiation pattern satisfactorily from +20 to -20 degrees. Whereas, the CF2 plot displays cogent similarity with the simulated results, although, it is asymmetric in nature.

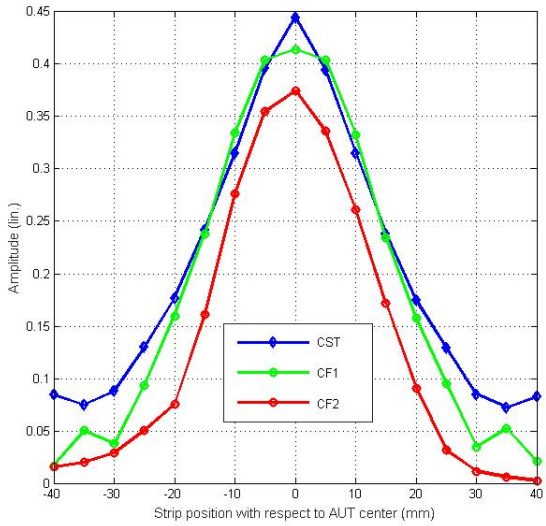


Figure 10: Reflection coefficients for horn antenna simulated and retrieved using CF1 and CF2 at 30 GHz.

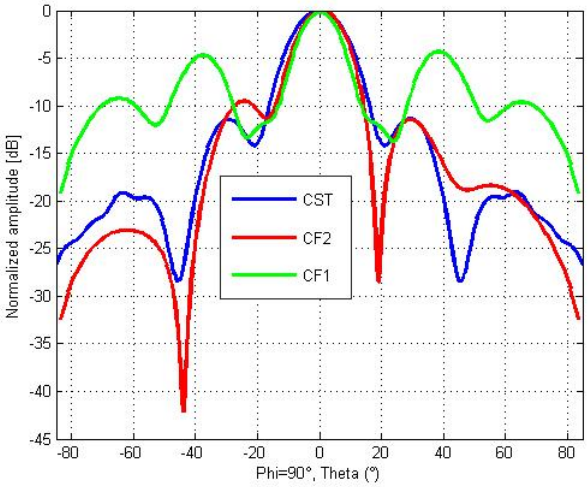


Figure 11: Radiation pattern for horn antenna simulated and retrieved using CF1 and CF2 at 30 GHz.

The inversion algorithm is processed in MATLAB. The *fminunc* function is used find the minimum value of the cost-function ($\Delta$). The *fminunc* function [20] allows

to have number of options to evaluate the *fminunc* function. Figure 12 and Figure 13 display the reflection coefficients and retrieved radiation pattern for different number of evaluations of *fminunc*. The difference in the final result due to the number of evaluations is shown in Table 2.

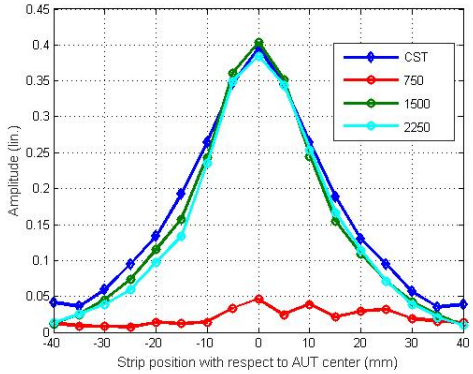


Figure 12: Reflection coefficient of horn antenna simulated and for 750, 1500 and 3000 evaluations at 30 GHz.

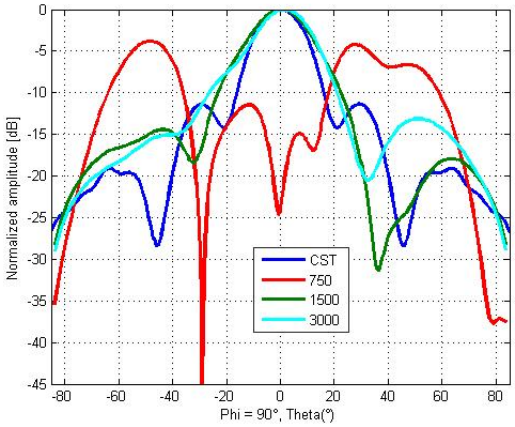


Figure 13: Radiation pattern for horn antenna simulated and for 750, 1500 and 3000 evaluations at 30 GHz.

Table 2: Influence of number of evaluations on $\Delta$

| **Number of evaluations** | $\Delta$ $(10^{-6})$ |
|---|---|
| 750 | 466.48 |
| 1500 | 3.41174 |
| 3000 | 0.344834 |

A few of the options used in this case are, TolX, i.e., step size or the difference between the current value of the $\Delta$. The cost-function used is CF2, in this case. Similar post-processing is done, with different $X_{move}$ limits, such as -60 mm to 60 mm and -46 mm to 46 mm. One more iteration to the options for *fminunc* is, increasing the number of function evaluations and specifying the iterated final CF value TolFun to be very low. Figure 14 and 15, display reflection coefficients and radiation pattern when TolX= $10^{-4}$, TolFun= $10^{-6}$ and number of evaluations = $10^6$.

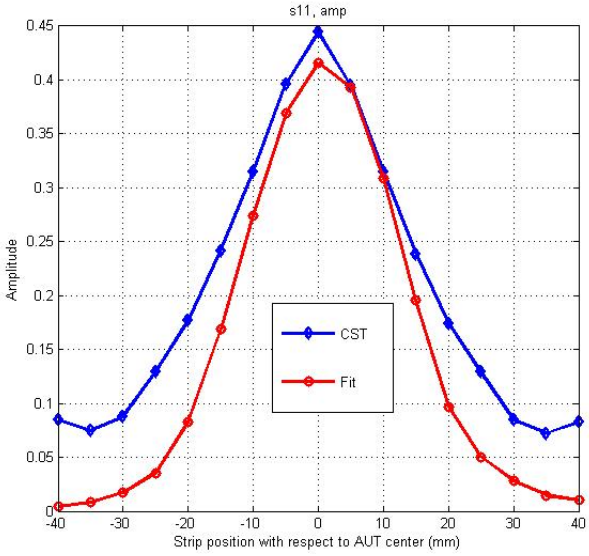


Figure 14: Reflection coefficient of horn antenna at 30 GHz with TolX = $10^{-4}$, TolFun = $10^{-6}$ and number of evaluations = $10^6$.

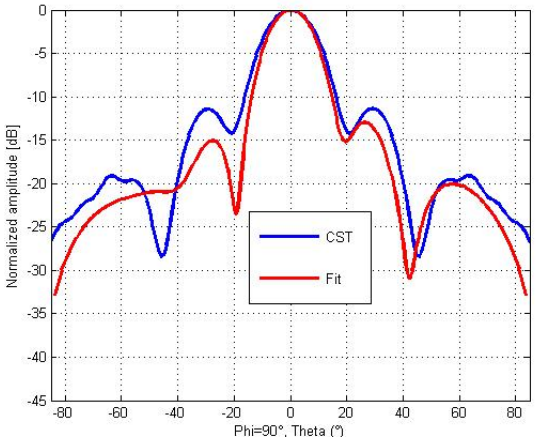


Figure 15: Radiation pattern of horn antenna at 30 GHz with TolX = $10^{-4}$, TolFun = $10^{-6}$ and number of evaluations = $10^6$.

# 3 Multiple reflection mitigation

Multiple reflections can cause problems in antenna measurement. The multiple reflected waves can interfere constructively or destructively. These can cause amplitude changes in the $S_{11}$. To reduce their effect, we perform measurements in an anechoic chamber. On-wafer antenna measurements are done on a probe station. The probe station has low portability for frequent placement in different rooms. Hence, it is unreasonable to place it in an anechoic chamber to perform radiation measurements and then, move it to another area afterwards.

The RPR method explained in Chapter 2 requires accurate measurement of reflection coefficients. The minimization of the cost-function leads to estimating the radiation pattern. Inadvertently, the accuracy of the estimated radiation pattern depends on the accuracy of the reflection coefficient. As the probe station is placed in a non radiation absorbing environment, a lot of multiple reflections occur. Figure 16 shows the probe station setup for the AUT measurement. The small rectangular brick is the AUT, the rectangular copper strip above the AUT is the reflecting plane. The copper strip is attached to the translation stage. Also seen in this figure, are the other sources of reflection apart from the reflecting plane.

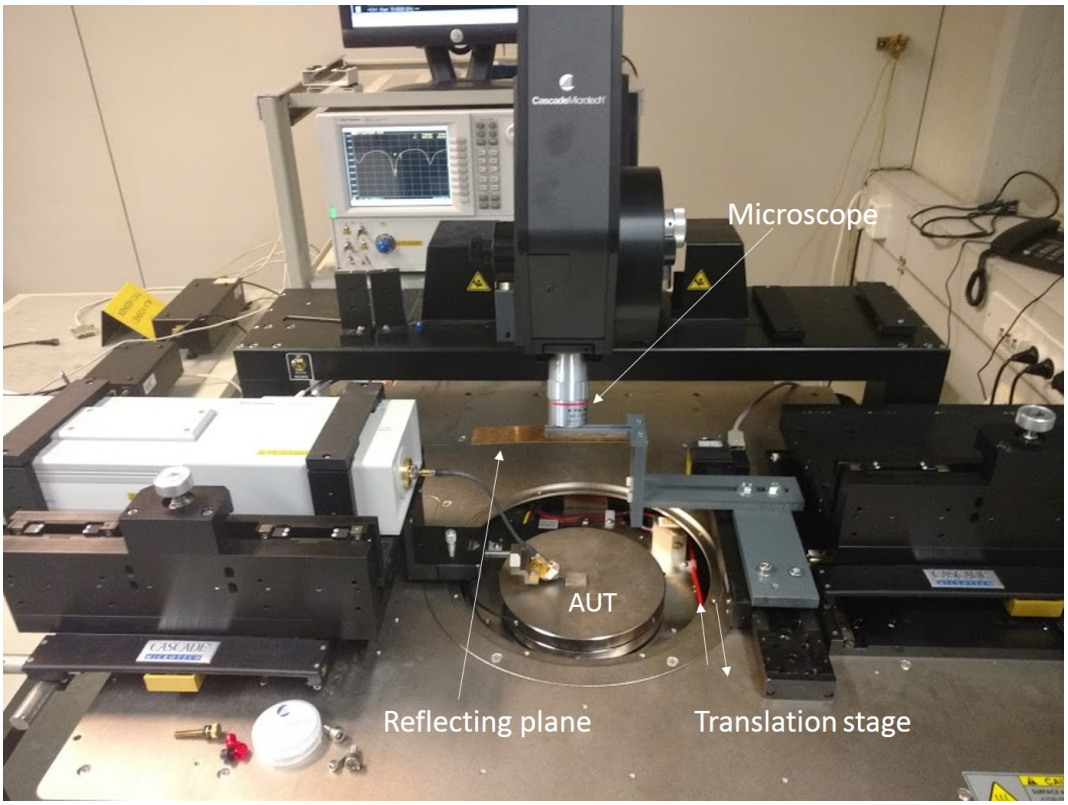


Figure 16: Probe station setup with translation stage.

A partial solution is to place absorbing material around the AUT, to negate reflections due to the base of the probe station and the surrounding. Even in this case, there can be delayed and multiple reflections from other appendages on the

station. For example, the microscope, and the translation stage can reflect and diffract the signal causing changes in the reflection coefficient. In overview, getting rid of multiple reflections for antenna measurements on the probe station using physical additions and configuration, can be quite challenging.

This chapter discusses post-processing methods to mitigate the effect of multiple reflections. This will allow the measurement setup to be simple, compact and easy to install. In this method, a time domain signal is gated and processed upon. Gating means the truncation of the signal to predetermined boundaries. The truncation of the signal is usually done by using a window. Time gating is achieved by multiplying the time signal available, with a window, of predetermined size, to get the desired time gated signal. Time gating is a small but significant part of this method. The signal is time gated precisely to include only the time signal with the first reflection.

In this thesis, the time gating method is first implemented for the results of the horn antenna, to test the method, and then expanded to the on wafer antenna. The first step is to simulate a CST model of the horn antenna and reflective strip setup as shown in Chapter 2. PEC is used in the CST simulation as the reflective strip, to speed up the computation time. Copper strip represents the reflecting strip in experiments. CST can reproduce the time domain signals which are reflected back to the input port.

In Figure 17, the time domain signals obtained from CST are visualized. In CST, the excitation signal for the setup can be chosen. By default, it is a Gaussian pulse defined by the frequency and bandwidth of simulation. The green plot here, is the excitation signal. The blue plot is the signal reflected back to the horn antenna feed when the reflective strip is at the $X_{move} = 0$ position. This plot will be addressed as center reflection position (CRP). The reflection due to the copper strip is observed at about 1.2 nanoseconds [21]. The red plot shows the reflected signal, when no reflective strip is placed in the vicinity of the horn. This time domain signal will further be addressed as free space response (FSR). The red plot attributes to the $S_{11,static}$. Two peaks are observed in the free space response. These two peaks are account for the impedance mismatch in the transition from the waveguide to the start of the horn and from the horn aperture, respectively [21]. The impedance mismatch can be removed by subtracting FSR from CRP. The term FSR is technically not correct. In a real experimental setup, the antenna is not placed in free space. But, it is used here to distinguish from the reflected signal received, when a reflective load is placed in front of the horn. The subtracted signal gives the final signal, canceling out the impedance mismatches due to the horn geometry. Figure 18 shows the difference in the reflection coefficients due to the subtraction.

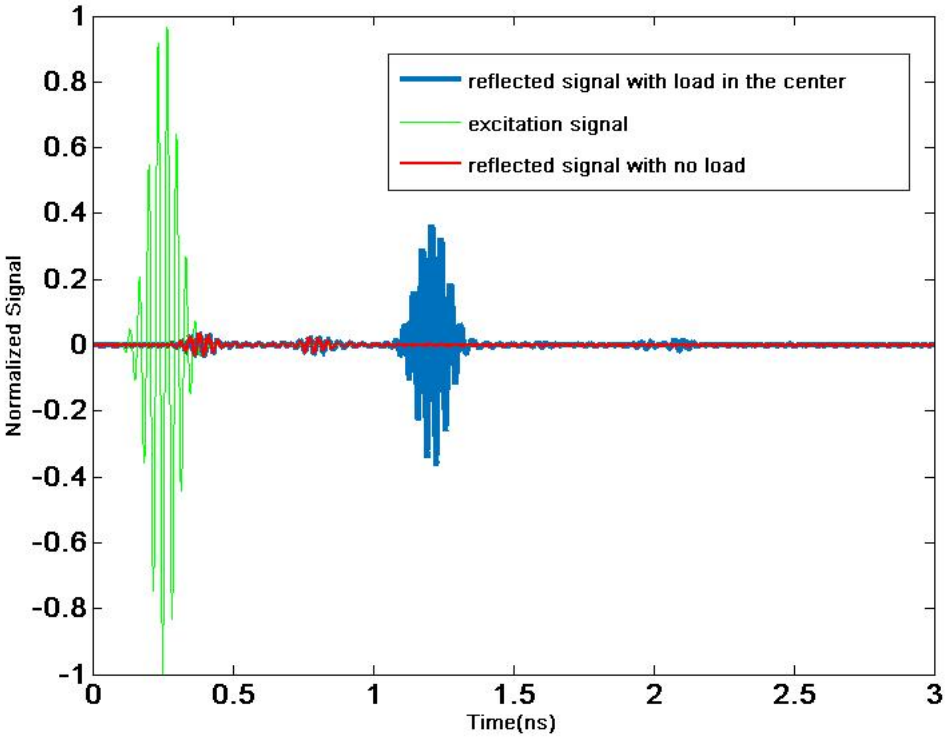


Figure 17: Time domain signals obtained from CST [21].

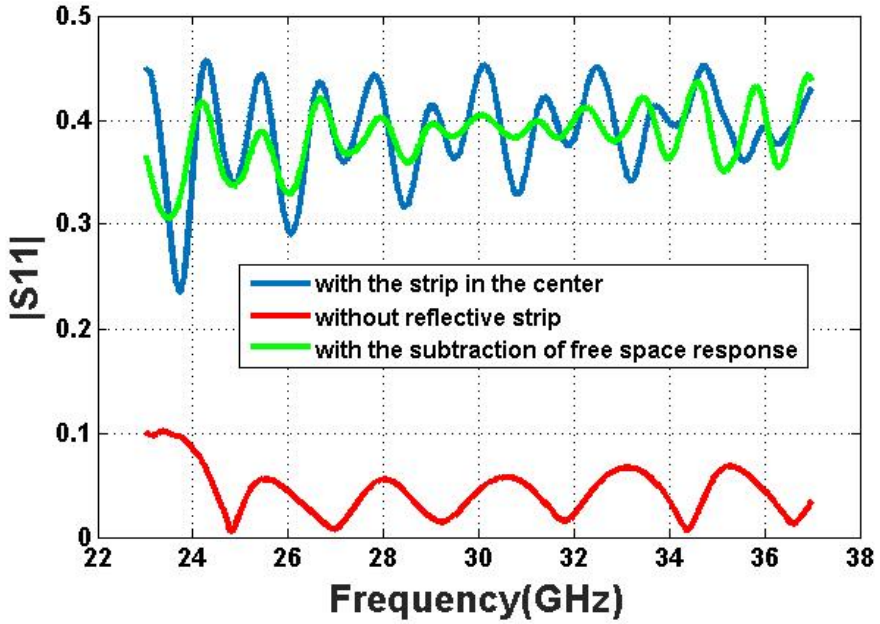


Figure 18: Reflection coefficients of the horn antenna.

This final signal is then time gated to isolate the first reflection due to the copper

strip. Time gating is multiplying the time domain signal with a gating window. The gating window is chosen according to the time duration required. This signal is then Fourier transformed to get the $S_{11}$ and should essentially, give the reflection coefficient of only the first reflection due to the strip. This method requires the time domain signal available, to carry out the process.

In case of experimental verification of this method, the Vector Network Analyzer (VNA) gives the reflection characteristics in the frequency domain, i.e., $S_{11}$. Hence, it becomes necessary to extract the time domain signal from the reflection coefficients. The reflection coefficients are inverse Fourier transformed to extract the time domain signals. As the horn antenna simulation results are already available, it is logical to use the $S_{11}$ from these results. The time domain signal is then extracted from reflection coefficients. The extracted time signal is compared with the time domain signal obtained from CST. On attaining a level of visual similarity, the free space response is subtracted from the one with the reflective strip, time gated and Fourier transformed. The reflected signal with the free space response and without the free space response are displayed in Figure 19 and Figure 20. The removal of reflection due to impedance mismatch, caused by the antenna geometry, can be clearly observed.

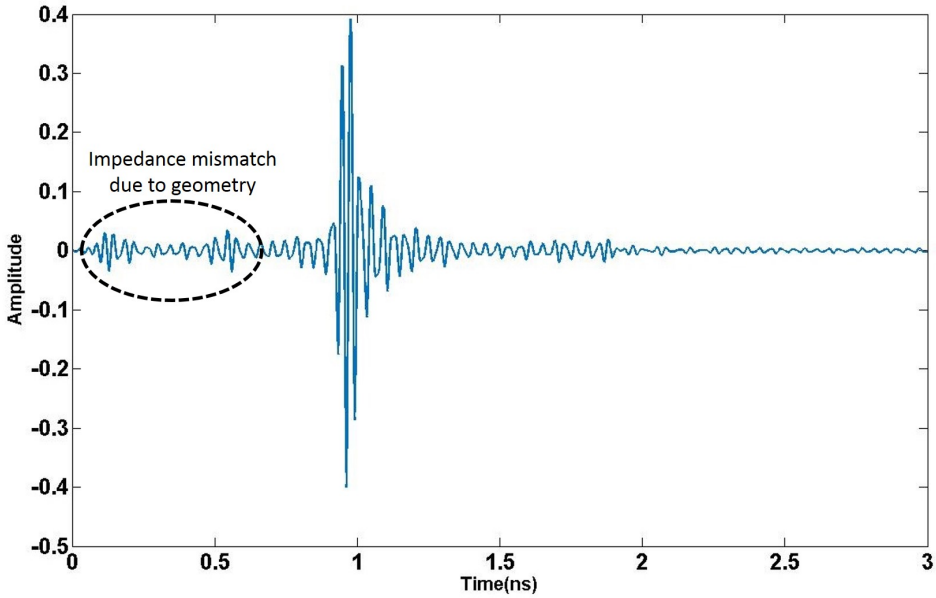


Figure 19: Time domain signal obtained from $S_{11}$ for 25-35 GHz bandwidth with free space response.

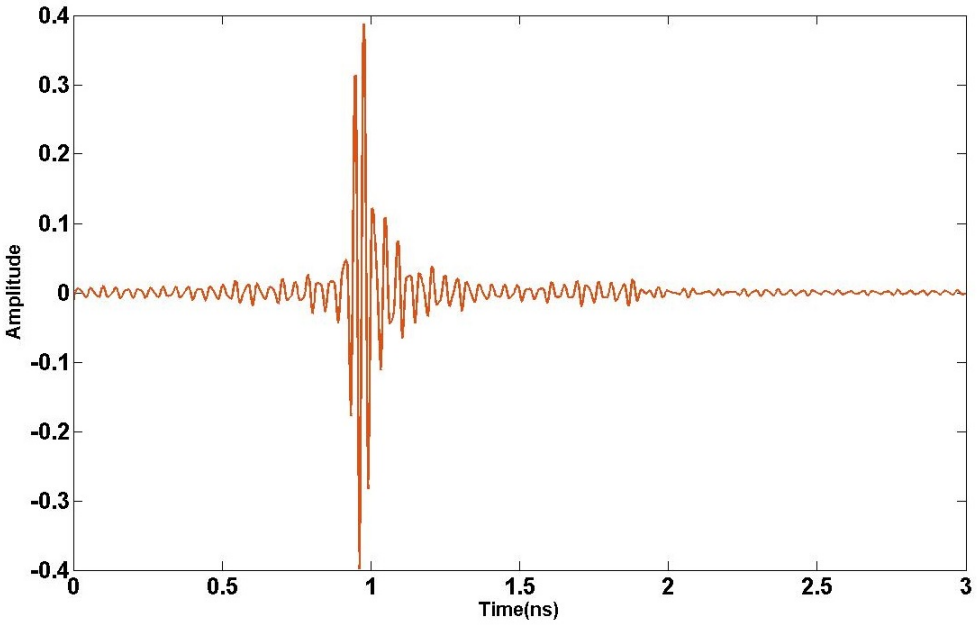


Figure 20: Time domain signal obtained from $S_{11}$ for 25-35 GHz bandwidth with free space response subtracted.

Figure 21 displays the flowchart of the multiple reflection mitigation process.

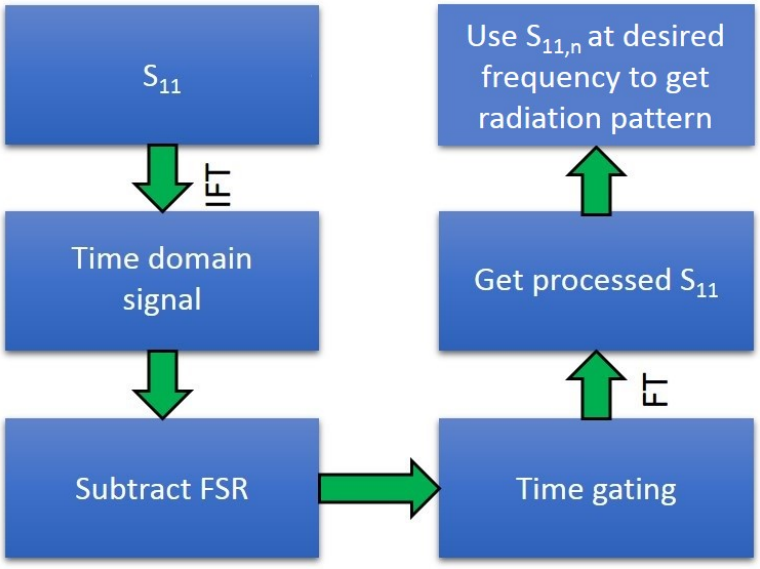


Figure 21: Flowchart of multiple reflection mitigation process.

The reflected signal is time gated at 1.5 ns. Figure 22 compares the reflection coefficients between the reflected signal and the time gated signal for two cases: 1) Free space response is included 2) Free space response is removed. As observed, if the free space response is not removed, reflection coefficient for the reflected signal and the time gated signal show similar behavior, although with amplitude differences at various frequencies. For the free space response removed case, reflection coefficient plots have smaller amplitude variations. The reflection coefficients for time gating and without time gating situation in FSR removed case, do not show plot similarity as is in the FSR included case. This results proves that the multiple reflection mitigation process does bring about a change in the reflection coefficient, hence showing that multiple reflections do affect the reflection coefficient value.

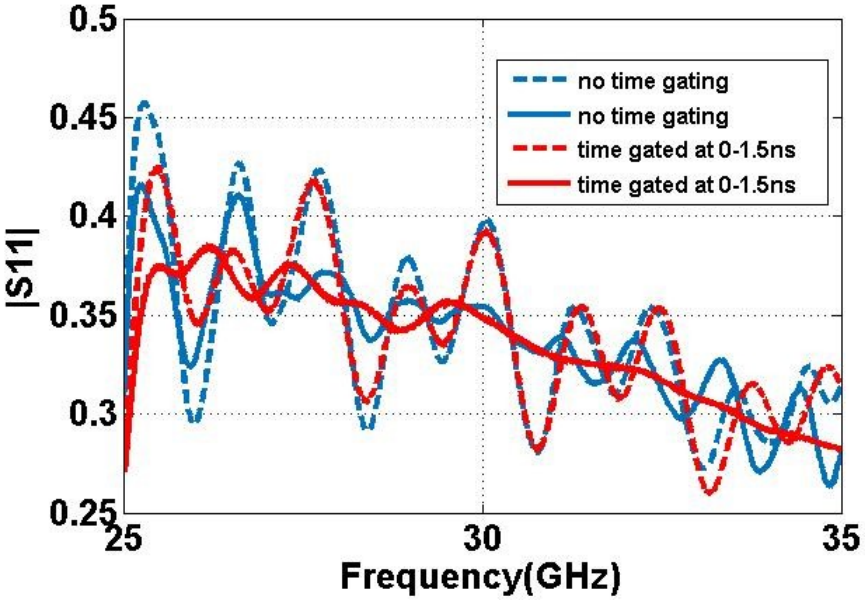


Figure 22: Reflection coefficients from extracted signals: free space response included (dashed) and free space response removed (solid).

# 4 On-wafer antenna

The thesis is done to focus on the implementation radiation pattern retrieval method on on-wafer antennas. Hence an antenna for experimental purposes, i.e., a 4x4 patch array is designed. 77 GHz is the frequency at which automotive radars are designed to operate. The patch array design has a directive radiation pattern compared to the almost isotropic radiation pattern of a patch antenna. The RPR method showed reasonable convergence for the main lobe of the horn, as shown in Figure 9, 11, 13 amd 15.

First step was to design a patch antenna, then move onto the 1x4 patch array and finally the 4x4 array. Patch antenna was designed according to the equations shown below [22],

$$\frac{W}{h} > 1 \tag{11}$$

$$\epsilon_{reff} = \frac{\epsilon_r + 1}{2} + \frac{\epsilon_r - 1}{2}[1 + 12\frac{h}{W}]^{-\frac{1}{2}} \tag{12}$$

$$\frac{\Delta L_p}{h} = 0.412\frac{(\epsilon_{reff} + 0.3)(\frac{W}{h} + 0.264)}{(\epsilon_{reff} - 0.258)(\frac{W}{h} + 0.8)} \tag{13}$$

$$L_{eff} = L_p + 2\Delta L_p \tag{14}$$

$$L_{eff} = \frac{1}{2f_r\sqrt{\epsilon_{reff}}\sqrt{\epsilon_0\mu_0}} \tag{15}$$

where $W$ is the width of the patch, $h$ is the substrate thickness, $L$ is the length of the patch, $f_r$ is the resonant frequency, $\epsilon_{reff}$ is the effective dielectric constant. The input impedance of the patch changes according to the width of the patch. The length and width of the patch are obtained using the equations and then adjusted. The input impedance of the antenna is higher than 50 Ω. Table 3 shows how the impedance and the resonant frequency of the antenna changes with dimensions. The initial values from which the dimensions are adjusted are as follows: $f_r$ = 77 GHz, $W_p$ = 1.54 mm, $L_p$ = 1.237 mm, and Z = 144 Ω.

Table 3: Patch dimension iteration process

| | $L_p$ (mm) | $W_p$ (mm) | Z (Ω) | $f_r$ (GHz) |
|---|---|---|---|---|
| Initial values | 1.237 | 1.54 | 144 | 77 |
| | 1.2 | 1.54 | 136.32 | 79.13 |
| | 1.2 | 1.6 | 126.57 | 79.05 |
| | 1.2 | 1.9 | 90.611 | 78.68 |

Coplanar probe has the impedance of 50 Ω. A 50 Ω microstrip line [23] is designed in the beginning to attach to the quarter wave transformer. Once the quarter-wave transformer [23] is designed, the 50 Ω microstrip line is replaced by a coplanar waveguide (CPW) [24]. This is because the coplanar probe can only interact with the on-wafer antenna using the CPW. The CPW design took a lot of iterations to design. The Air-coplanar probe that is to be used has a probe pitch of 100 $\mu$m [14]. The pitch of the probe is the centre to centre distance of the probe tips. This restriction causes design problems for the CPW.

CPW characteristic impedance calculations are done as shown in [24]. The coplanar waveguide calculator [25] is used to assist in these calculations. The CPW impedance increases with decrease in the centre conductor width [24]. Decreasing the gap between the centre conductor and ground plane, however decreases the characteristic impedance. Furthermore, the minimum dimension that can be manufactured for the antenna is 50 $\mu$m, with considerable tolerance. Considering all these restrictions and requirements, the CPW is designed with the dimensions, shown in Figure 23,

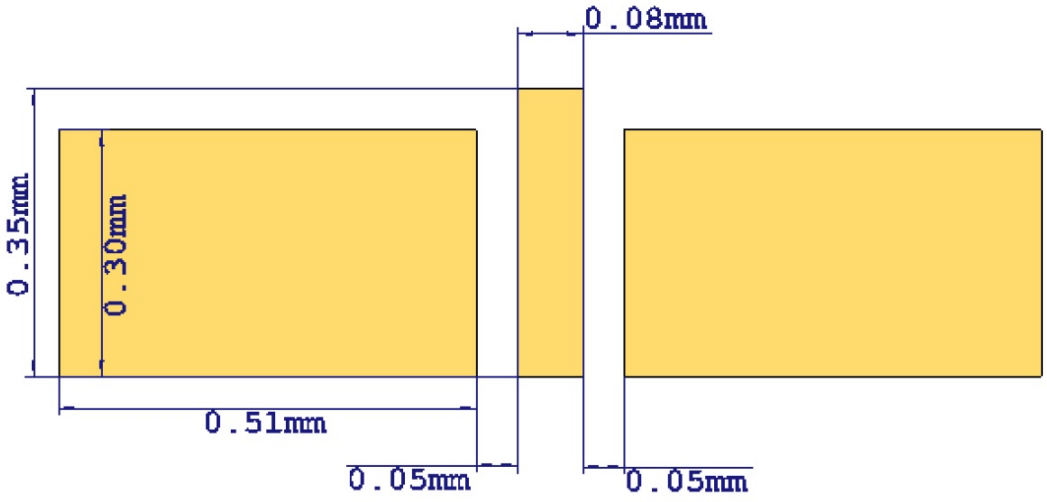


Figure 23: CPW section for feeding the antenna with a GSG probe.

The microstrip line from the CPW to the patch antenna is made long enough, so that the patch antenna is far away from the upper ground plane. This ensures that, the electric field does not couple to the upper ground plane and is primarily between the ground plane below the antenna. the microstrip line is adjusted later on for impedance matching. The same applies to the patch, which was calculated according to the formulae previously stated and then modified to get the required impedance matching and radiation pattern. CST time domain solver is used to determine that the required characteristics are fulfilled. The design is optimized to resonate at 77 GHz.

Table 3 mentions the common antenna parameters for all the three antennas. This includes the length of the on-wafer antenna, the width of the on-wafer antenna and height of the dielectric substrate. The substrate used for all three antennas is Rogers 5880 substrate [26]. The permittivity of the substrate is 2.2. The loss tangent is 0.0004.

Table 4: Common antenna parameters for patch, 1x4 array and 4x4 array

| **Parameter** | **Value (mm)** |
|---|---|
| Substrate thickness | 0.127 |
| Length of the antenna | 19 |
| Width of the antenna | 14 |
| Copper plating thickness | 0.018 |
| FR-4 thickness | 2 |

Figure 24 shows the lateral view of all on-wafer antennas. An FR-4 substrate is used as support for the antennas, as the thickness of the antenna substrate is very small. This FR-4 substrate does not affect the radiation pattern or impedance as it is attached below the ground plane of the antenna.

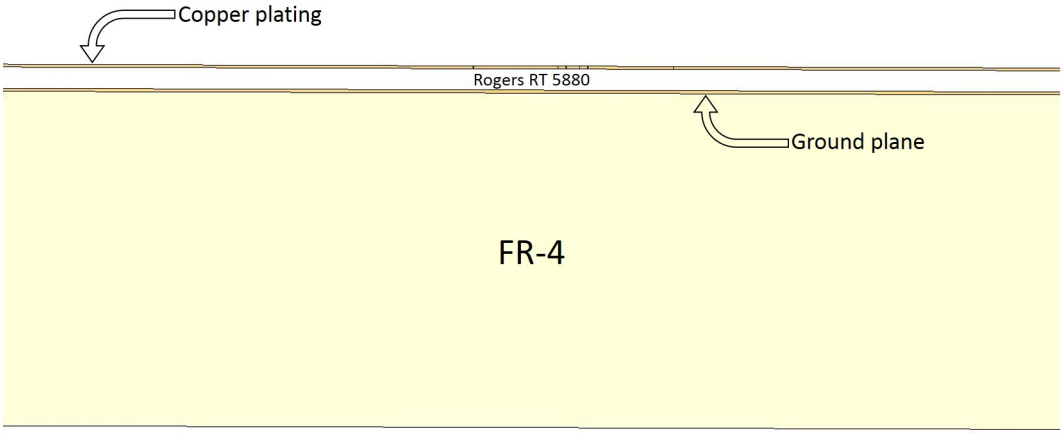


Figure 24: Lateral view of on-wafer antenna.

Figure 25 displays the geometry of the patch antenna. All the dimensions displayed in the figure are in mm. Figure 26 displays the 3D radiation pattern of the patch antenna.

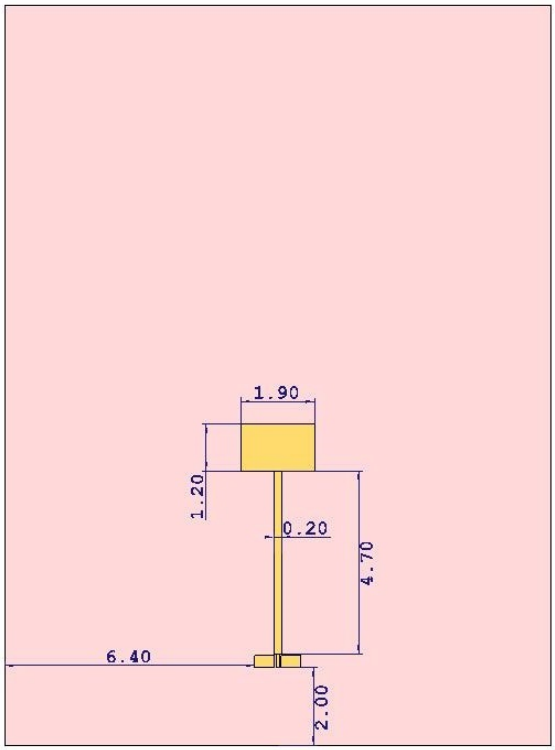


Figure 25: Patch antenna. All dimensions are in mm.

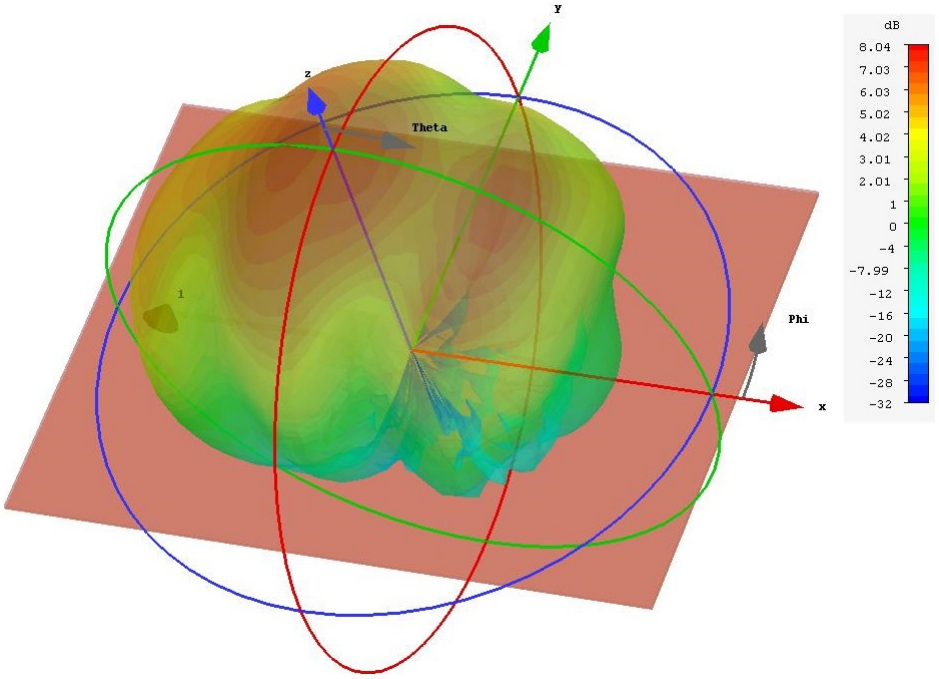


Figure 26: Patch antenna 3D radiation pattern.

Figure 27 displays the patch antenna radiation pattern in the cartesian co-ordinate system. The radiation pattern cut in the $\phi = 0°$ and $\phi = 90°$ plane is normalized.

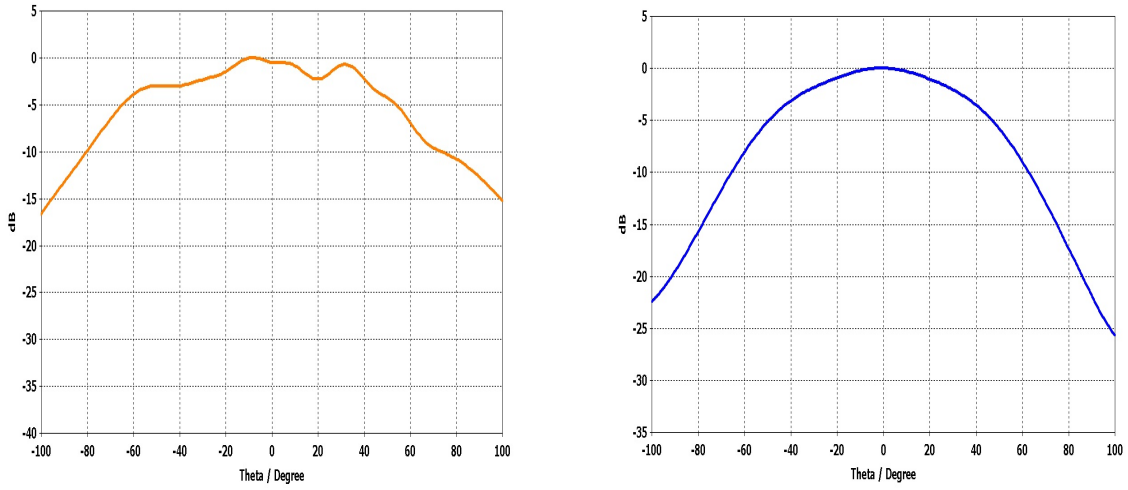


(a) (b)

Figure 27: Patch antenna radiation pattern in the cartesian co-ordinate system: (a)$\phi = 0°$, (b)$\phi = 90°$

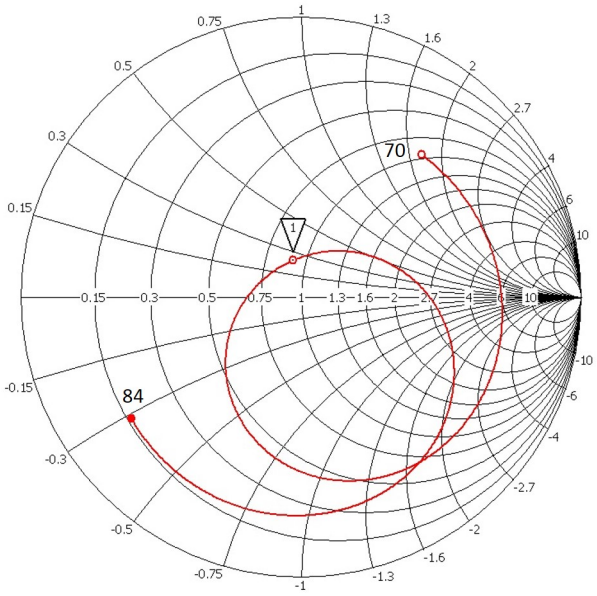


Figure 28: Reflection coefficient of the simulated patch antenna on a smith chart from 70 GHz to 84 GHz. (1) is at 77 GHz.

The next part after the patch antenna design is the 1x4 array design. The 1x4 array is designed as shown in Figure 29. The dimensions for the antenna are in mm. The array is constituted of 4 patches. First, each of the patches are connected by a quarter-wave transformer, i.e., 1.3 mm. The patches and the length of the connecting

stubs are iterated, to get the impedance and phasing correct. Figure 30 displays the 3D radiation pattern of the 1x4 patch array. The 1x4 array is directive in the $\phi = 0°$ plane.

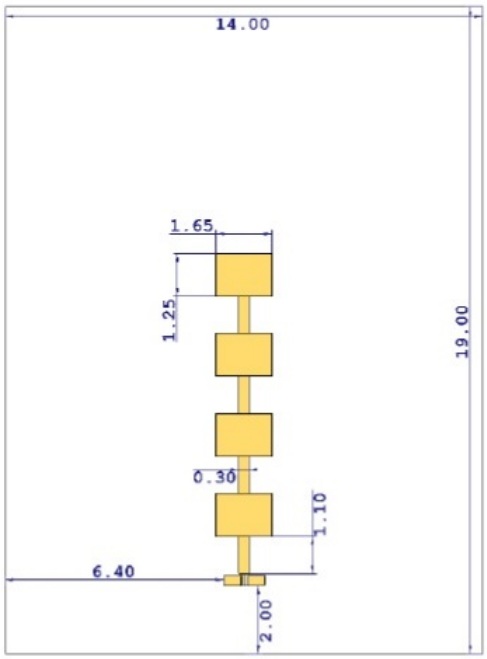


Figure 29: 1x4 patch array. All dimensions are in mm.

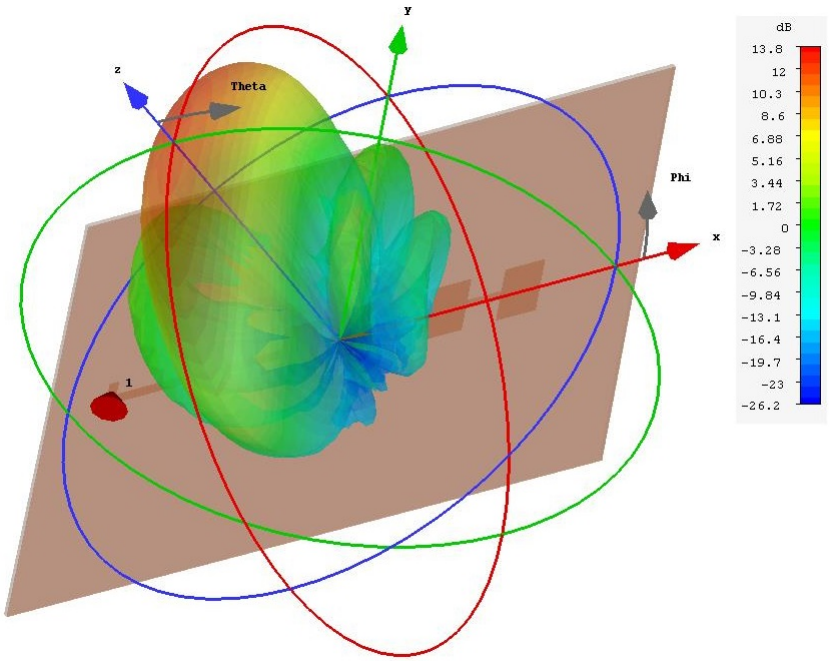


Figure 30: 1x4 patch array 3D radiation pattern.

Figure 31 displays the 1x4 patch array radiation pattern in the cartesian co-ordinate system. The radiation pattern cut in the $\phi = 0°$ and $\phi = 90°$ plane is normalized.

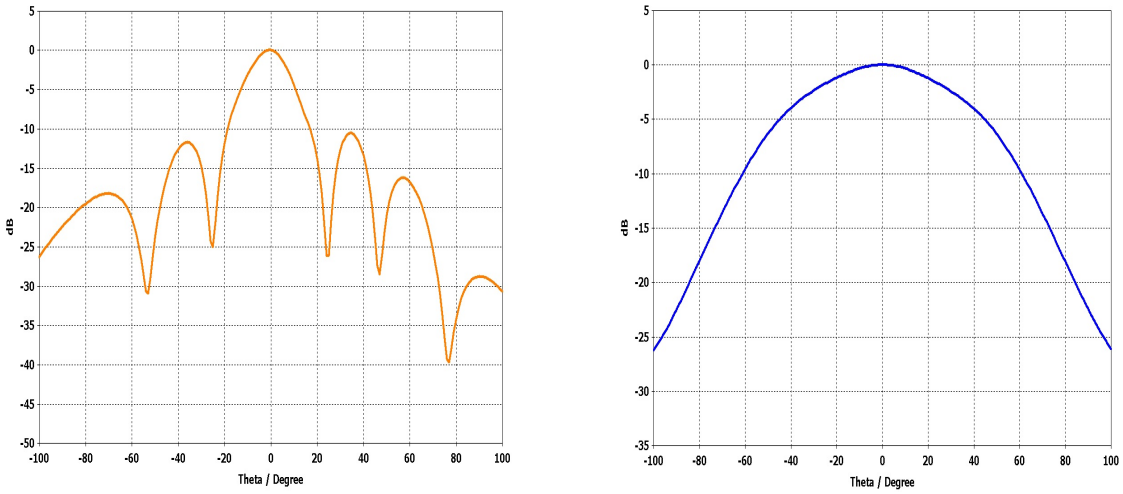


(a) (b)

Figure 31: 1x4 patch array radiation pattern in the cartesian co-ordinate system (a)$\phi = 0°$, (b)$\phi = 90°$.

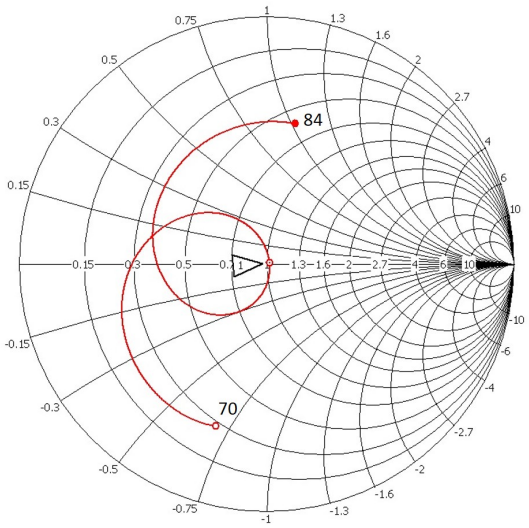


Figure 32: Reflection coefficient of the simulated 1x4 patch array on a smith chart from 70 GHz to 84 GHz. (1) is at 77 GHz.

The first step in designing the 4x4 patch array is to make a microstrip line which connects all the 4 branches of the array. The length of the line should be a multiple of $\lambda$, for having the same phase in all the branches. The rest of the design rules follow are similar to those for the 1x4 patch array. The distance of the array from the microstrip line is such that, the radiation pattern does not tilt. The distance

between the patches and the patch size themselves is adjusted according to the appropriate radiation pattern. Iterating and adjusting, the final 4x4 patch array design is achieved. Figure 33 displays the 4x4 patch array design. The dimensions mentioned are in mm. Figure 34 shows the 3D radiation pattern of the 4x4 patch array.

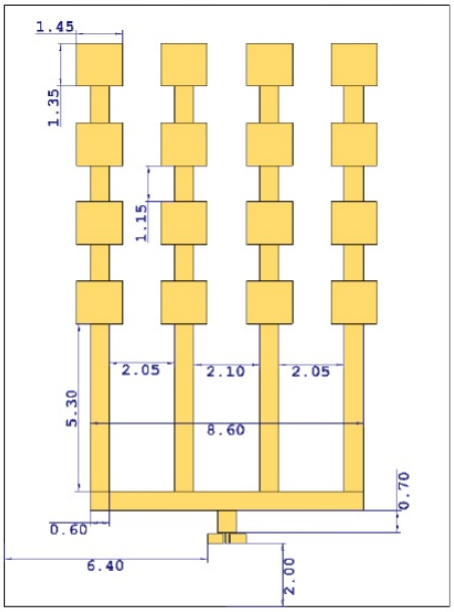


Figure 33: 4x4 patch array. All dimensions are in mm.

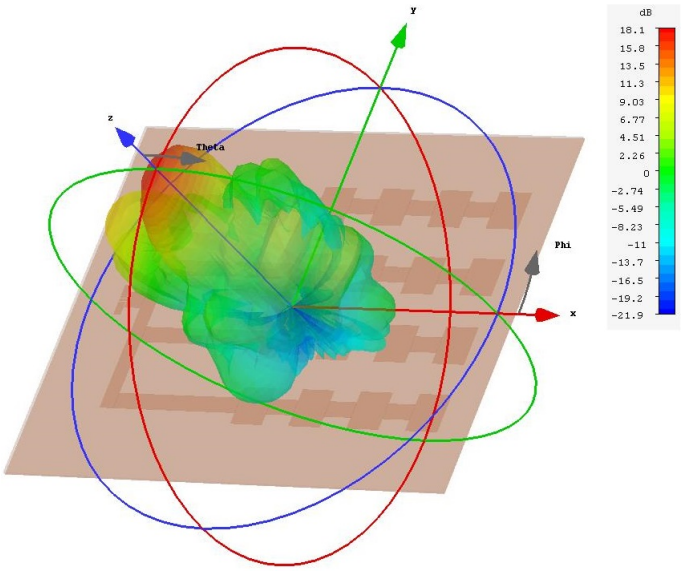


Figure 34: 4x4 patch array radiation pattern.

Figure 35 displays the 4x4 patch array radiation pattern in the cartesian co-ordinate system. The radiation pattern cut in the $\phi = 0°$ and $\phi = 90°$ plane is normalized.

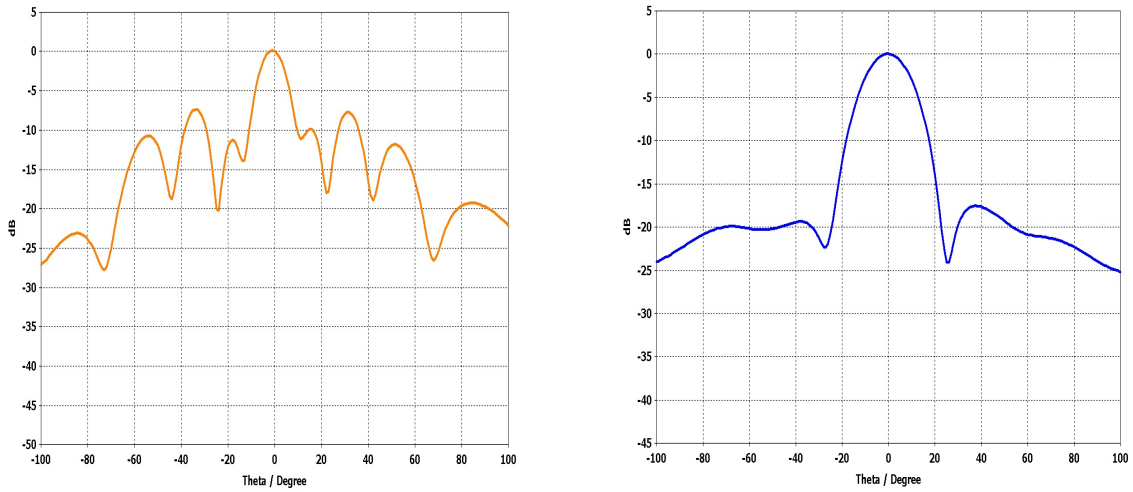


(a) (b)

Figure 35: 4x4 patch array radiation pattern in the cartesian co-ordinate system: (a)$\phi = 0°$, (b)$\phi = 90°$.

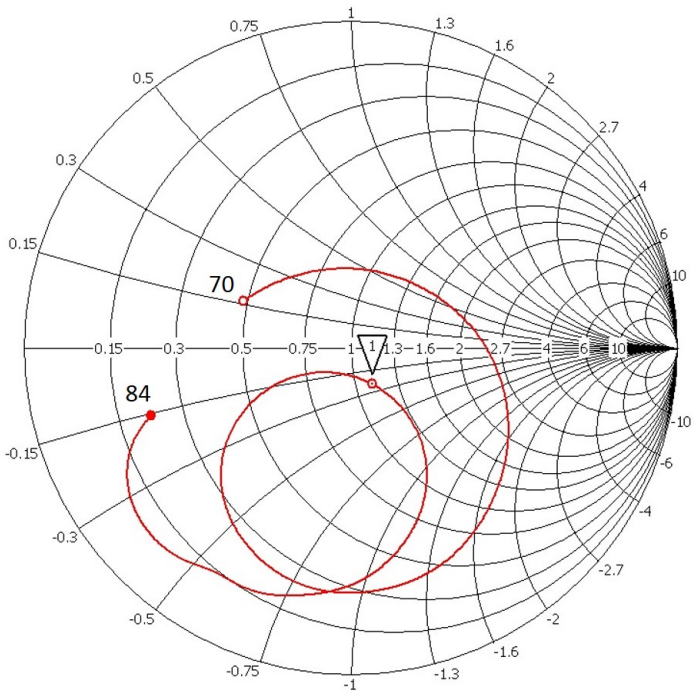


Figure 36: Reflection coefficient of the simulated 1x4 patch array on a smith chart from 70 GHz to 84 GHz. (1) is at 77 GHz.

# 5 Experiment and results

The antennas are designed and manufactured to operate at 77 GHz. The next step is perform the experiments and analyze the results. The 4x4 patch array, from chapter 4 is placed on the probe station chuck and $S_{11}$ is measured. The setup is shown in Figure 37. The experiment is performed, at different heights, 90 mm and 120 mm above the antenna. Two widths of the reflective strip are used: 30 mm and 60 mm are the widths used. The purpose of the different heights and width is to observe if the experiment gives the same results at these varied experimental setups.

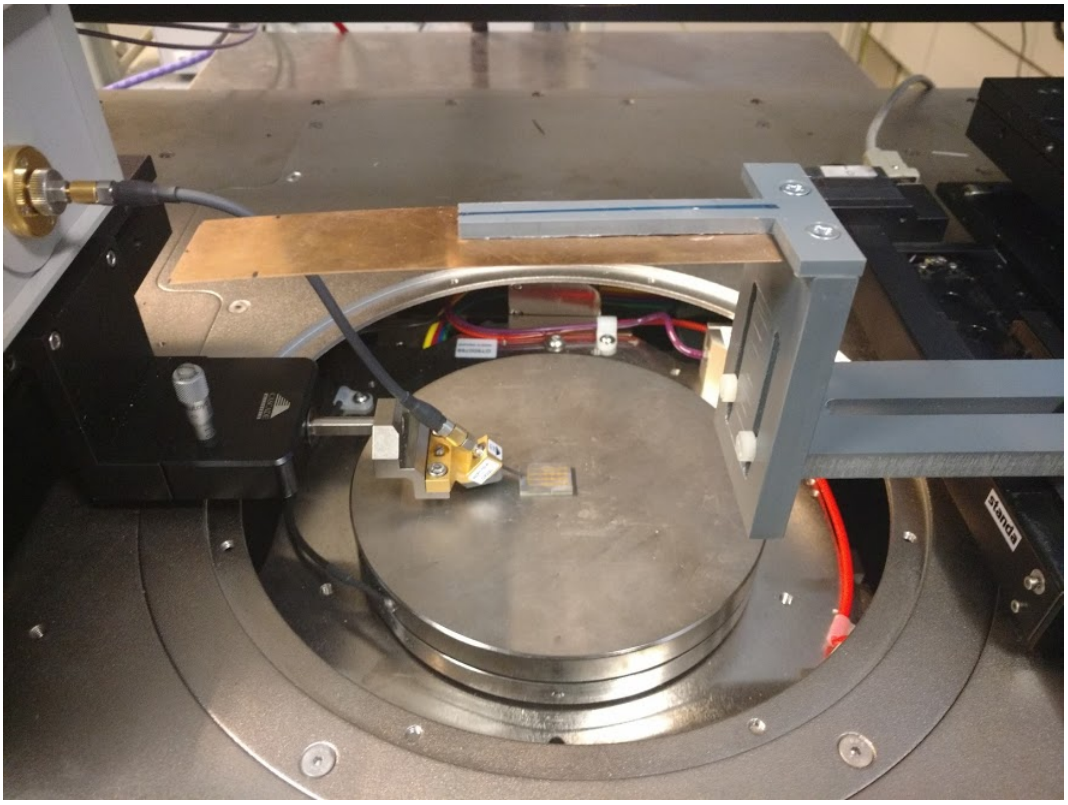

Figure 37: Experimental setup for on-wafer antenna measurement.

The first step is to measure $S_{11,static}$. $S_{11,static}$ is supposed to be measured in free space. The $S_{11,static}$ obtained from an ideal simulation of the antenna in CST is displayed in Figure 38. To account for the unwanted reflecting surfaces, $S_{11,static}$ is measured with the everything involved in the experimental setup, except the copper strip. Measured $S_{11,static}$ is compared with simulated $S_{11,static}$ in Figure 38. The shift in measured $S_{11,static}$ can be accounted to: (1) reflections from objects in the antenna vicinity as seen in Figure 37 and (2) manufacturing error in the fabrication of CPW. As the characteristic impedance of the CPW is sensitive to gap width, this manufacturing error causes the shift in measured $S_{11}$.

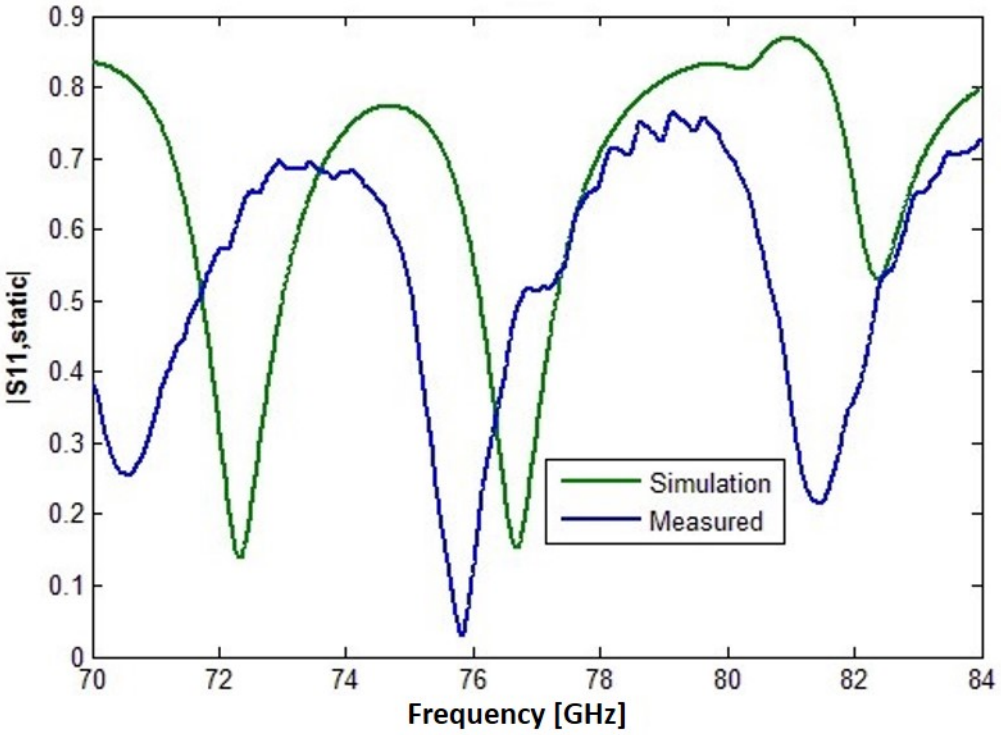


Figure 38: Simulated and measured $S_{11,static}$ for 4x4 patch array antenna.

The next step is to measure $S_{11,n}$. The translation stage is connected to a stepper motor which moves the platform. The platform translates the stepper motor movement to the copper strip appendage. This stage is controlled using LabView. The copper strip is moved from -39 mm to +39 mm in 1.95 mm ($\lambda/2$) steps.

The third step is to post-process the measurements. The time domain signals are created from the reflection coefficients and the free space response is subtracted from them.

Figure 39 display the contour plot of the reflection coefficients measured for the 4x4 patch array at different positions. Figure 39 (a) and (b) display $S_{11}$ when the copper strip width is 60 mm and the strip distance is 120 mm and 90 mm respectively. Figure 39 (c) and (d) display $S_{11}$ when the copper strip width is 30 mm and the strip distance is 120 mm and 90 mm respectively.

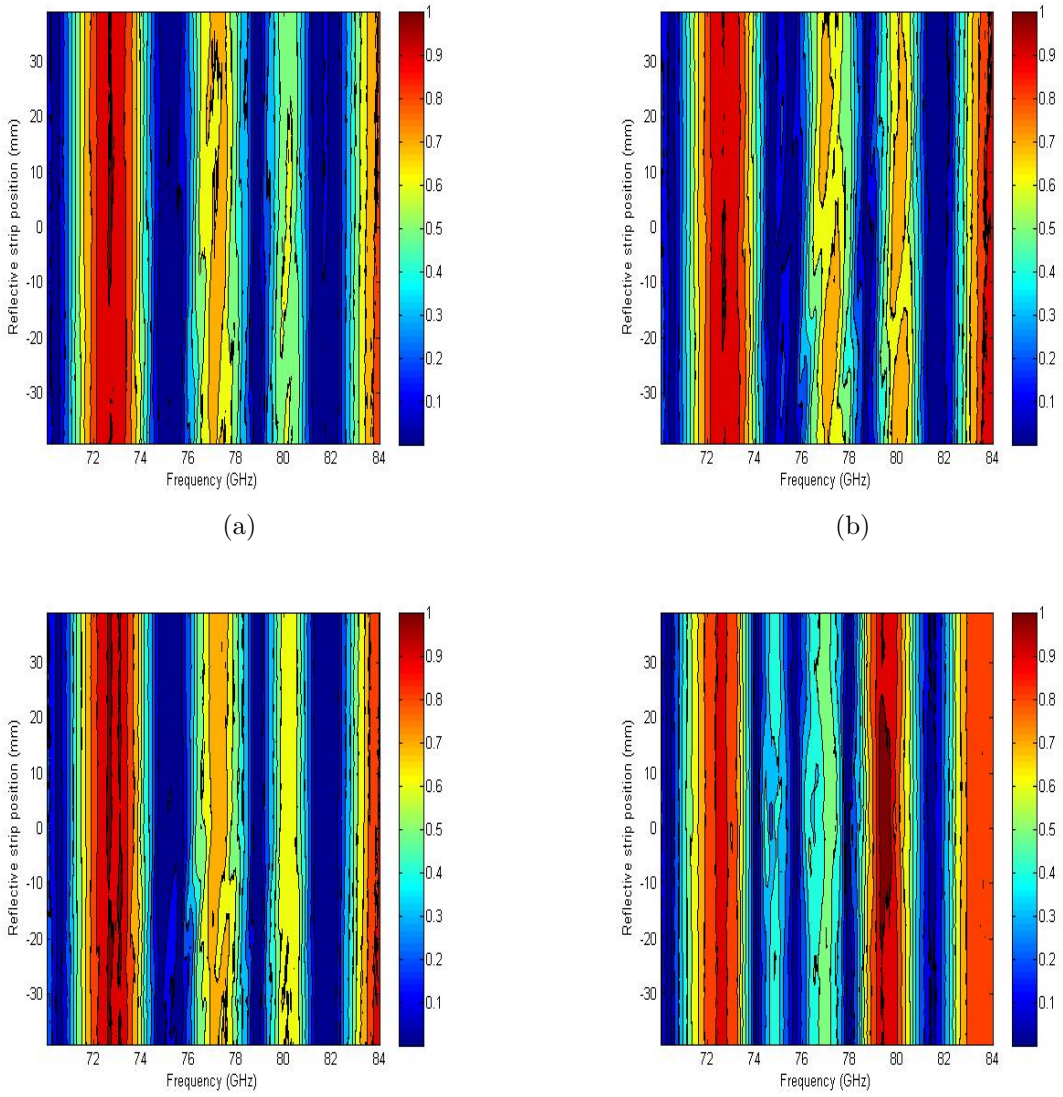


Figure 39: Original $S_{11}$ for 4x4 patch array with copper strip at: (a)$z_0 = 120$ mm, $W = 60$ mm (b)$z_0 = 90$ mm, $W = 60$ mm (c)$z_0 = 120$ mm, $W = 30$ mm and (d)$z_0 = 90$ mm, $W = 30$ mm

Time domains signal extracted from these reflection coefficients is displayed in Figure 40. Only Figure 40 (b) displays reflections in this time interval. The rest of the plots, do not cancel the $S_{11,static}$ time component properly, hence the remnants of these can be seen in Figure 41 (a), (c) and (d). A better method to correlate FSR and reflected signal is to be implemented to cancel out the $S_{11,static}$ component.

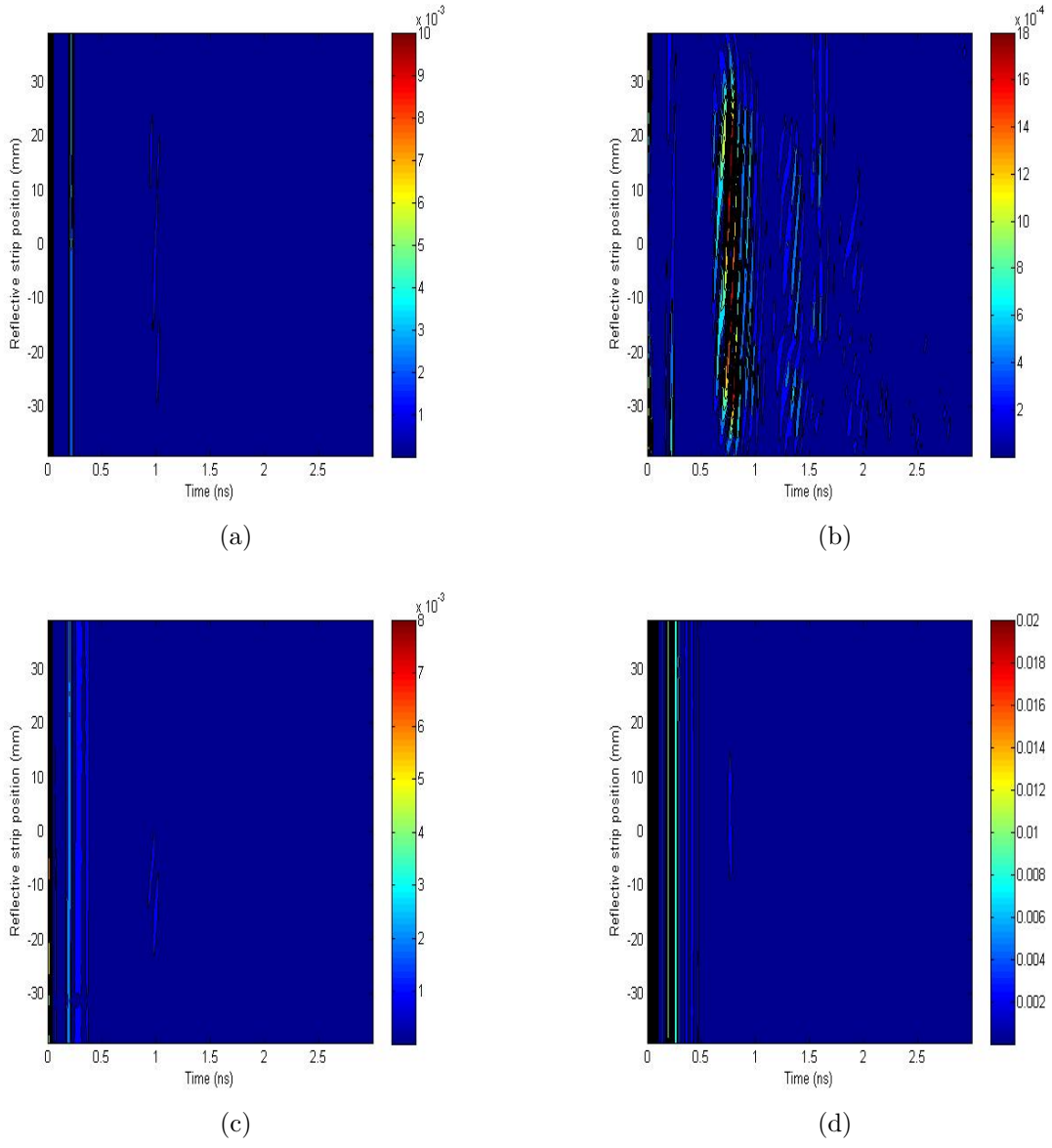


(a) (b)

(c) (d)

Figure 40: Reflected signal extracted from reflection coefficients with copper strip at: (a)$z_0 = 120$ mm, $W = 60$ mm (b)$z_0 = 90$ mm, $W = 60$ mm (c)$z_0 = 120$ mm, $W = 30$ mm and (d)$z_0 = 90$ mm, $W = 30$ mm

Based on an educated guess, from Figure 41 (b), all the time domain signals are time gated from 0.6-1.5 ns. This is a good approximation, based on the distance of the copper strip from the antenna. Figure 41 displays the time gated signal in the 0.6-1.5 ns interval.

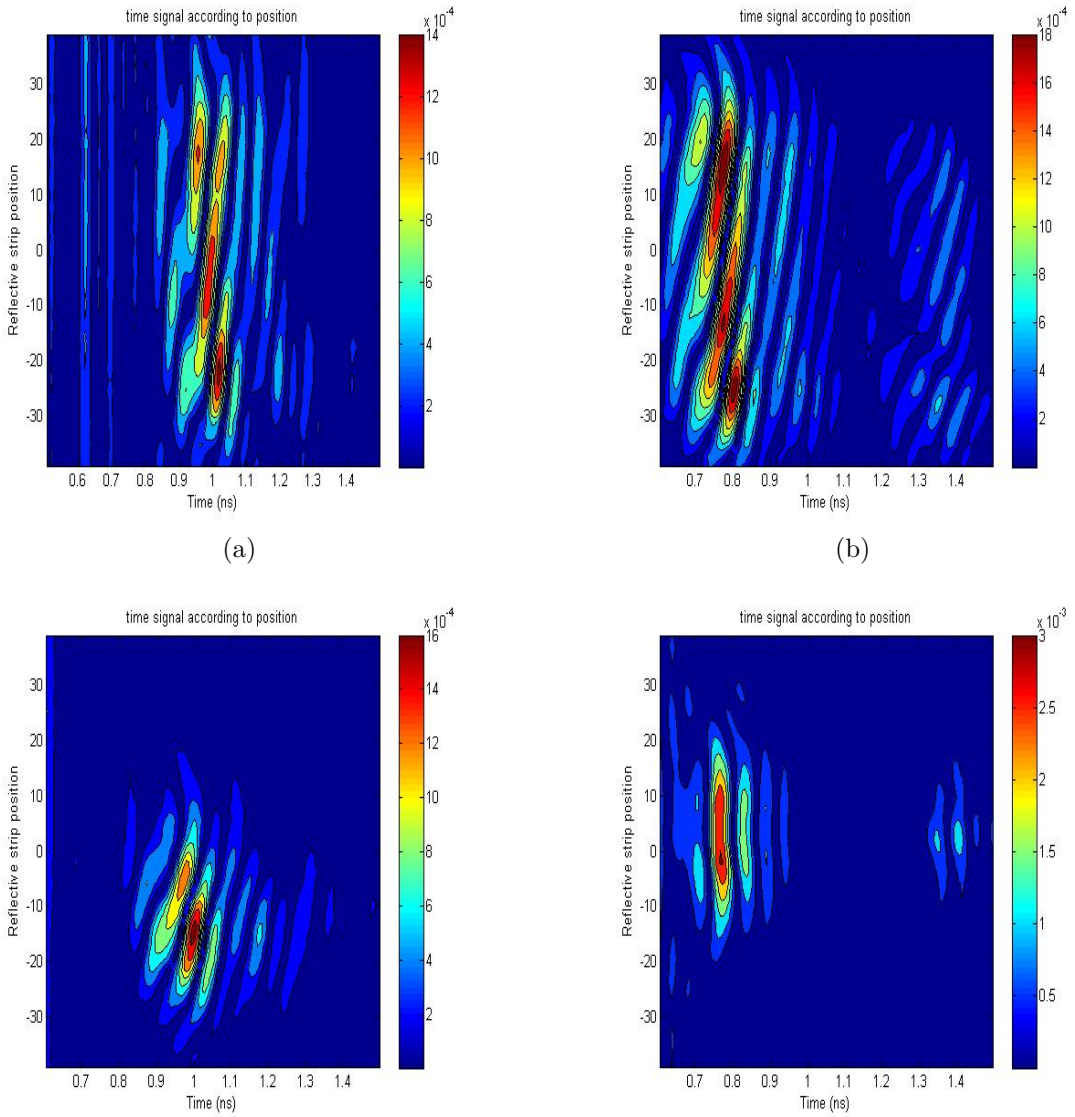


Figure 41: Time gated reflected signal for copper strip at: (a) $z_0 = 120$ mm, $W = 60$ mm (b)$z_0 = 90$ mm, $W = 60$ mm (c)$z_0 = 120$ mm, $W = 30$ mm and (d)$z_0 = 90$ mm, $W = 30$ mm.

Figure 42 displays the final reflection coefficients obtained from the time gated signal.

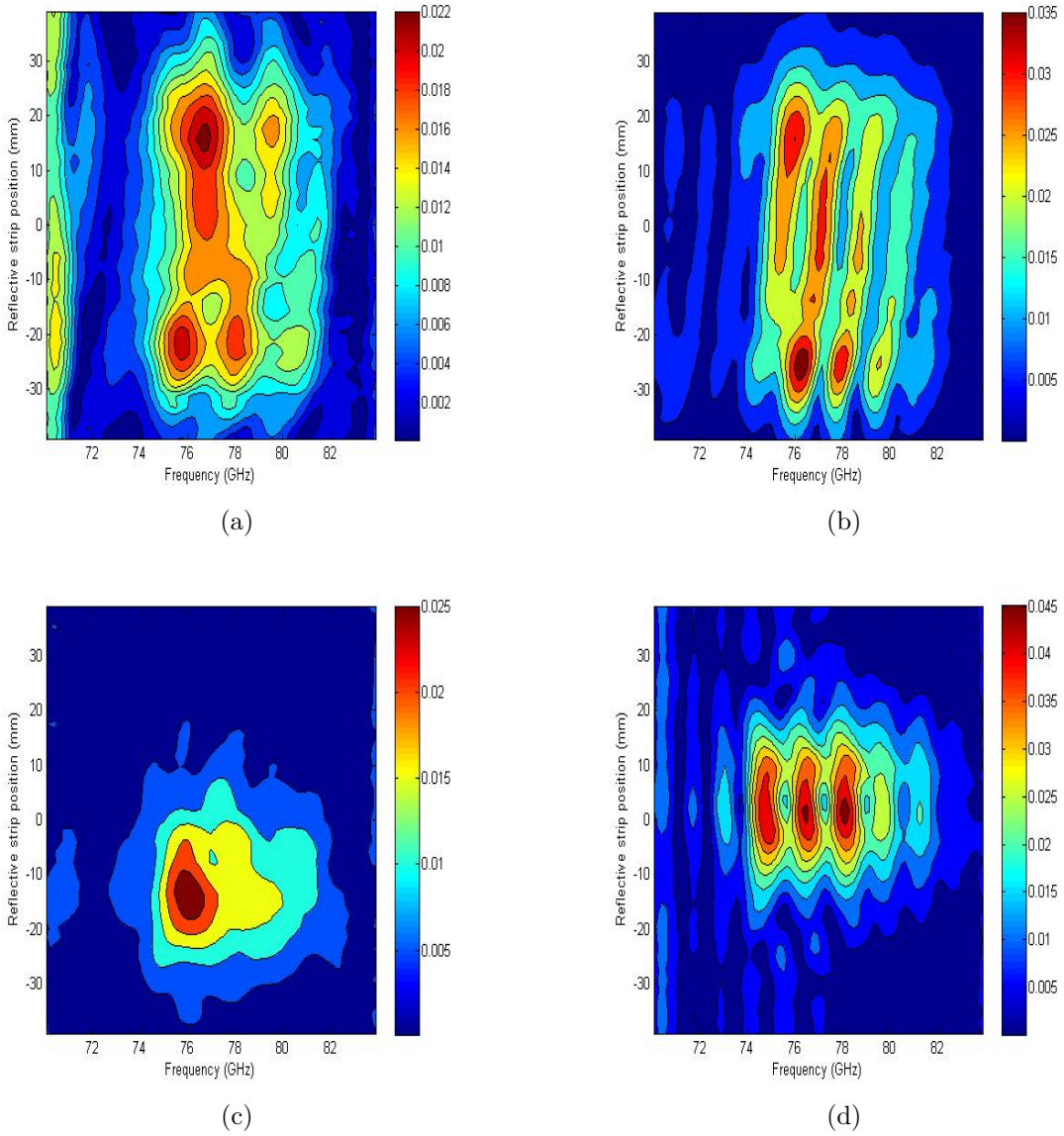


Figure 42: Final $S_{11}$ for copper strip at (a) $z_0 = 120$ mm, $W = 60$ mm (b)$z_0 = 90$ mm, $W = 60$ mm (c)$z_0 = 120$ mm, $W = 30$ mm and (d)$z_0 = 90$ mm, $W = 30$ mm.

Figures 43 displays reflection coefficient at a particular frequency and their corresponding fit using the RPR method. The reflection coefficients at a particular frequency for each case is decided based on the contour plots of the final $S_{11}$ presented in Figure 42. The reflection coefficient plot at different positions, is expected to peak at the zero position, i.e., directly in front of the antenna, and slope down on either sides of the zero position. This will support the idea of multiple reflection mitigation being implemented successfully. Reflection coefficients for the $z_0 = 90$ mm, $W = 60$ mm at 77.128 GHz and $z_0 = 90$ mm, $W = 30$ mm at 78 GHz seem to follow this trend.

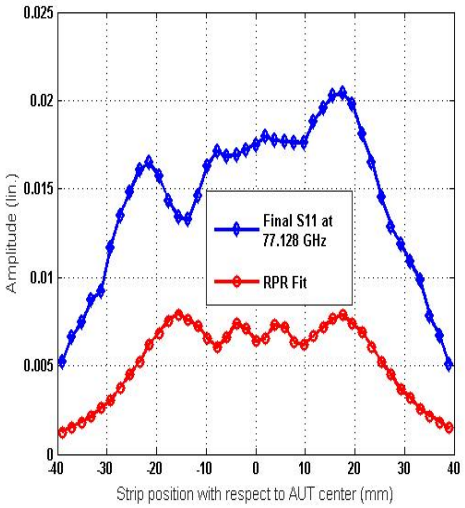


(a)

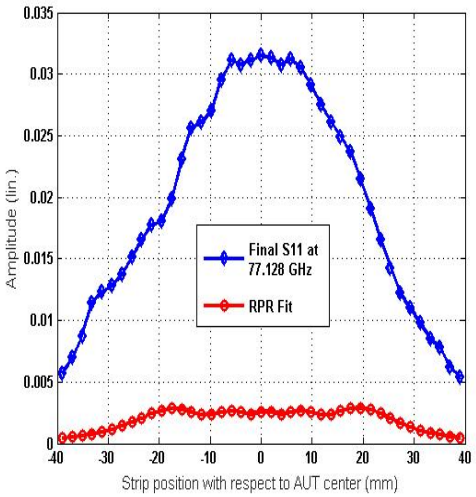


(b)

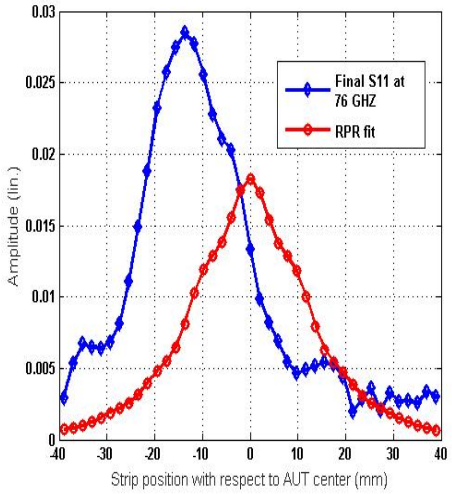


(c)

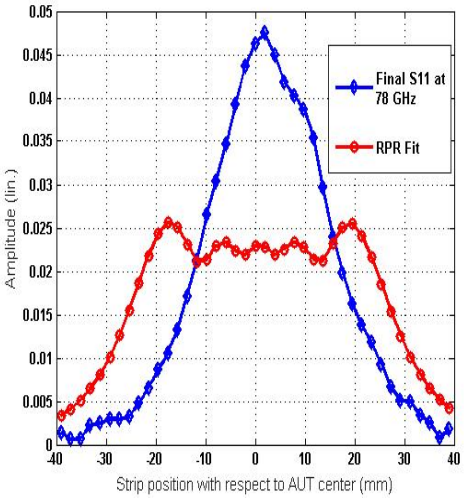


(d)

Figure 43: Final $S_{11}$.

Figure 44 compares the CST simulated radiation pattern of the 4x4 array at 77 GHz with a)$z_0 = 120$ mm, $W = 60$ mm at 77.128 GHz, b) $z_0 = 90$ mm, $W = 60$ mm at 77.128 GHz c) $z_0 = 120$ mm, $W = 30$ mm at 76 GHz and $z_0 = 90$ mm, $W = 30$ mm at 78 GHz.

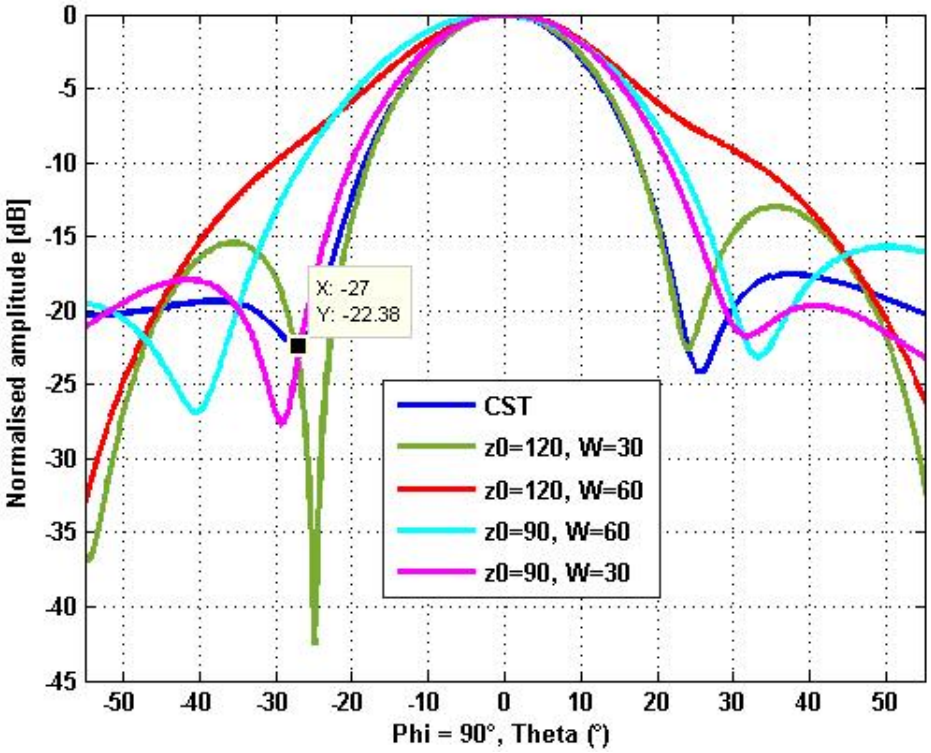


Figure 44: Radiation pattern in $\phi = 90°$ plane retrieved from the following reflection coefficients: (a)CST simulation (b)$z_0 = 120$ mm and $W = 30$ mm (c)$z_0 = 120$ mm and $W = 60$ mm (d)$z_0 = 90$ mm and $W = 60$ mm (e)$z_0 = 90$ mm and $W = 30$ mm.

As observed in case of the horn antenna simulation, the RPR method combined with the multiple reflection mitigation process, gives good agreement with the main lobe of the simulated radiation pattern. In the $z_0 = 120$ mm, $W = 60$ mm case, the retrieved radiation pattern is quite dissimilar from the simulated radiation pattern of the 4x4 array. For the $z_0 = 120$ mm, $W = 30$ mm case, the radiation pattern displays good agreement for the width of the main lobe. The radiation pattern displays asymmetric behavior after the main lobe. The $z_0 = 90$ mm, $W = 60$ and $z_0 = 90$ mm, $W = 30$ show the same behavior, with good agreement for the main lobe and deviation from the simulated pattern after the first null. In all the cases of the retrieved radiation pattern, the cost-function value is high, as can be seen from Figures 43 (a) - 43 (d). Hence, even though multiple reflections have been alleviated in $z_0 = 90$ mm, $W = 60$ mm at 77.128 GHz and $z_0 = 90$ mm, $W = 30$ mm at 78 GHz case, the radiation pattern plots suggest the requirement of more analysis of the radiation pattern retrieval method and multiple reflection mitigation process.

# 6 Summary

The objective of this thesis was to implement the RPR method in a probe station environment for a GSG probe feeding an on-wafer antenna, and attempt to mitigate the effects of multiple reflection for this method. Chapter 2 presents the various antenna measurement methods and explains how RPR method attempts to overcome the problems to measure on-wafer antennas in the mm-wave frequency range. The RPR method does not require complicated mechanical arms to measure on-wafer antennas in the far-field and negates the phase inaccuracy problem in the near-field measurement method. The procedure of the RPR method is explained along with previous work done regarding it. The inversion algorithm required to implement the RPR method was executed in MATLAB. A horn antenna designed to operate at 30 GHz, is used to test the radiation pattern retrieval theory.

Different limits are applied to the *fminunc* function, used to find the minimum value of the cost-function, to see how the method works. First off, the retrieved radiation pattern is compared, for two cost functions, CF1 and CF2. The radiation pattern due to both the cost-functions shows good agreement for the main lobe. But, CF1 deviates from the radiation pattern near the +/- 20° mark, while the CF2 radiation pattern shows pattern agreement upto +/- 40°. The *fminunc* function, used to calculate minimum $\Delta$, can be used to set different limits to get varying levels of accuracy. Increasing the number of evaluations of the cost-function from 750, 1500 to 3000, gives better agreement as observed in Figure 13. Figure 15, displays the radiation pattern retrieved by changing additional limits of the *fminunc* function, namely, TolX, which defines the minimum step size, TolFun, which defines the minimum value of the iterated cost-function and number of evaluations of the function. Observing the radiation pattern results in chapter 2, the input of additional limits to the *fminunc* function has improved the agreement between the simulated and retrieved radiation pattern. Hence, in chapter 5, these limits are used to retrieve radiation pattern for on-wafer antenna.

Chapter 3 focuses on mitigating the multiple reflections, to improve radiation pattern received. The radiation patterns in Chapter 2, which display agreement upto +/- 40°, are obtained from CST simulations as also the reflection coefficients. In CST, an ideal environment is simulated. In reality, especially for on-wafer probe-fed antennas, using a probe station, a lot of reflections from the surroundings occur. Figure 14, displays the source of these reflections. Chapter 3, shows the step by step process of multiple reflection mitigating process. Time gating is used for this purpose. Figure 20 shows the changes in reflection coefficients, due to the process described in Chapter 3. The reflection coefficients smoothen due to the removal of the free space response.

Chapter 4 delves into the design and manufacture of the 4x4 on-wafer array antenna. Here, the steps between the design evolution of the patch antenna to the 1x4 array to the 4x4 array are mentioned. The GSG CPW restriction due to the probe pitch and manufacturing error, required many iterations to attain proper impedance matching at 77 GHz.

Experiments and simulations similar to those for the horn antenna are carried

out on the 4x4 on-wafer patch array. These experiments, simulations and their results are discussed in chapter 5. The frequency shift in the reflection coefficient between measurement and simulation is most likely due to the manufacturing error and multiple reflections. Figure 38 displays the shift in $S_{11,static}$. Figures 39-42 show the results of the process to obtain reflection coefficients after time gating, which can then be used in the RPR method. Figure 43 displays the reflection coefficients for different frequencies, which are then used to retrieve the radiation pattern shown in Figure 44.

Although it is expected that the time gating removes multiple reflections from the reflective strip to the antenna and the stray reflections due to the probe station environment, the radiation pattern comparison at the end of Chapter 5, provides inconclusive proof of the reliability of multiple reflection mitigation using time gating process and radiation pattern retrieval along with inversion algorithm. This process needs to be studied further. A good way to proceed would be to use different time gating windows and observe their effects. A wide bandwidth antenna would help to reduce impedance mismatch due to antenna manufacturing errors. Other methods to mitigate multiple reflection as mentioned in [27] could be implemented with RPR method. The inversion algorithm used to implement RPR method needs to be tested exhaustively and a method to determine the parameters fed into the algorithm needs to be developed.

# References


[1] L. Frenzel, "Millimeter waves will expand the wireless future," [Online] Available: http://electronicdesign.com/datasheet/millimeter-waves-will-expand-wireless-future-pdf-download. Visited: 12/2015

[2] P. Adhikari, "Understanding millimeter wave wireless communication," [Online] Available: http://www.loeacom.com/pages/support_downloads.htm. Visited: 12/2015.

[3] Y. Ozturk and F. Ustuner, "Design and realization of a planar near field antenna measurement system," *2011 XXXth URSI General Assembly and Scientific Symposium,*, Istanbul, 2011, pp. 1-4.

[4] A.D. Yaghjian, "An overview of near-field antenna measurements," *IEEE Transactions on Antennas and Propagation,* vol. 34, no.1, pp. 30-45, January 1986.

[5] Z. Du, V. Viikari, J. Ala-Laurinaho, A. Tamminen, and A.V. Räisänen, "Antenna pattern retrieval from reflection coefficient measurements with reflective loads," *Progress In Electromagnetics Research,* vol. 148, pp. 15-22, 2014.

[6] M. Winebrand, J. Aubin, and R. Soerens, "Applications of time domain processing in antenna measurements," [Online] Available: http://www.microwavejournal.com/articles/9839-applications-of-time-domain-processing-in-antenna-measurements?v=preview. Visited: 05/2016.

[7] "Compact antenna test range (CATR) based on a hologram," [Online] Avaialble: http://radio.aalto.fi/en/research/projects/compact_antenna_test_range-catr-based _on_a_hologram-002/. Visited: 05/2016.

[8] Z. Du, "Development of Characterization Methods for Antennas and Quasi-Optics," *Aalto University publication series DOCTORAL DISSERTATIONS,* 8/2015.

[9] "Infinity Probe," [Online] Available: https://www.cascademicrotech.com/products /probes/rf-microwave/infinity-probe. Visited: 05/2016.

[10] T. Zwick, C. Baks, U. R. Pfeiffer, D. Liu, and B. P. Gaucher, "Probe based mmw antenna measurement setup," *IEEE Antennas and Propagation Society International Symposium,* 2004, vol. 1, pp. 747-750.

[11] J.A.G. Akkermans, R. van Dijk and M.H.A.J. Herben, "Millimeter-wave antenna measurement," *Proceedings of the 37th European Microwave Conference,* October 2007, Munich Germany, pp. 83-86.

[12] S. Beer and T. Zwick, "Probe based radiation pattern measurements for highly integrated millimeter-wave antennas," *Proceedings of the Fourth European Conference on Antennas and Propagation,* 12-16 April 2010, pp. 1-5.

[13] S. Ranvier, M. Kyrö, C. Icheln, C. Luxey, R. Staraj, and P. Vainikainen, "Compact 3-D on-wafer radiation pattern measurement system for 60 GHz antennas," *Microwave and Optical Technology Letters,* vol. 51, No. 2, pp. 319-324, February 2009.

[14] "Probe Selection Guide," Cascade Microtech.

[15] D.E.N. Davies and M.J. Withers, "New approach to compact measurements on reflector antennas," *Electronic Letters,* Vol. 17 No. 25, pp. 960-961, 10th December 1981.

[16] M. Hoque, M.S. Smith, and D.E.N. Davies, "Compact gain measurements on reflector antennas," *Microwaves, Optics and Antennas, IEE Proceedings H,* vol. 131, No. 6, pp. 371-378, December 1984.

[17] T. Calazans, H.D. Griffiths, A.L. Cullen, D.E.N. Davies and R. Benjamin, "Antenna radiation pattern measurement using a near-field wire scattering technique," *IEE Proceedings - Microwaves, Antennas and Propagation,* vol. 145, No. 3, pp. 263-267, June 1998.

[18] J. Ala-Laurinaho, Z. Du, V. Viikari, and A. V. Räisänen, "Radiation pattern retrieval from impedance measurement with a reflective object in the antenna near field," *CAMA,* 16-19 Nov. 2014, pp. 1-2.

[19] V. Viikari, Z. Du, V. Semkin, J. Ala-Laurinaho and A. V. Räisänen, "Reflection coefficient method for characterizing antennas on probe stations," *9th European Conference on Antennas and Propagation,* Lisbon, 2015, pp. 1-4.

[20] "Fminunc:Find minimum of unconstrained multivariable function," [Online] Available: http://se.mathworks.com/help/optim/ug/fminunc.html?search Highlight=fminunc. Visited: 11/2015.

[21] G. Khairkar, J. Ala-Laurinaho, V. Viikari, V. Semkin, and A. V. Räisänen, "Mitigation of multiple reflections in antenna pattern retrieval method," *10th European Conference on Antennas and Propagation,* 10-15 April 2016.

[22] C. A. Balanis, *Antenna Theory Analysis and Design,* Third Edition, Wiley-Interscience, 2005.

[23] D. M. Pozar, *Microwave Engineering,* Fourth Edition, Wiley, 2012.

[24] R. N. Simons, *Coplanar Waveguide Circuits, Components and Systems,* Wiley-Interscience, 2001.

[25] "Coplanar Waveguide Calculator," [Online] Available: http://www.microwaves101.com/encyclopedias/coplanar-waveguide-calculator. Visited: 11/2015.

[26] "RT/duroid® 5870 / 5880," [Online] Available: https://www.rogerscorp.com/documents/606/acs/RT-duroid-5870-5880-Data-Sheet.pdf. Visited: 10/2015.

[27] J. Ala-Laurinaho, Z. Du, V. Semkin, V. Viikari and A. V. Räisänen, "Reflection coefficient method for antenna radiation pattern measurements," *European Radar Conference (EuRAD),* Paris, 2015, pp. 285-288.